2

Analytical Models for Microstrip Antennas

2.1 Introduction

Various types of microstrip radiators, their applications, radiation mechanisms, models for various types of feeds, and the basic antenna characteristics were discussed in Chapter 1. Analysis of the antenna is carried out in this chapter. Antenna analysis is important for several reasons, including these:

- It can reduce the number of costly cut-and-try cycles by aiding the design process.
- Analysis can be used to ascertain the advantages as well as limitations of the antenna by carrying out parametric studies.
- Analysis can provide an understanding of the operating principles that could be useful for a new design, for modifications to an existing design, and for the development of new antenna configurations.

The objectives of antenna analysis are to predict the radiation characteristics such as radiation patterns, gain, and polarization as well as near-field characteristics such as input impedance, impedance bandwidth, mutual coupling, and antenna efficiency. The analysis of microstrip antennas is complicated by the presence of dielectric inhomogeneity, inhomogeneous boundary conditions, narrow frequency band characteristics, and a wide variety of feed, patch shape, and substrate configurations. Thus, a balance is reached between the complexity of the method and the accuracy of solution by compromising one

or more of the features listed above. The resulting model is said to be a *good* model if it has the following characteristics [1]:

- It can be used to calculate all impedance and radiation characteristics of the antenna under discussion.
- Its results are accurate enough for the intended purpose.
- It is as simple as possible, while providing the proposed accuracy for the impedance and radiation properties.
- It lends itself to interpretation in terms of known physical phenomena.

Many elaborate techniques have been proposed and used to determine microstrip antenna characteristics. The analytical techniques include the transmission line model, generalized transmission line model, cavity model, and multiport network model. These techniques maintain simplicity at the expense of accuracy. Full-wave methods have received increasing attention due to their rigor and higher accuracy. These are, in general, based on Sommerfeld-type integral equations, and the solution of Maxwell's equations in the time domain. Prominent numerical methods include integral equation analysis in the spectral domain, integral equation analysis in the space domain, and the finite-difference time-domain (FDTD) approach. The methods based on integral equation make one important assumption: The dielectric substrate and the ground plane are infinite in extent. The solutions are therefore more accurate when the substrate and ground plane are several wavelengths long. The FDTD technique is more efficient for finite-sized antennas. The effect of finite size is less severe on impedance behavior because microstrip antennas are inherently resonant structures and their impedance characteristics are primarily determined by the patch. The radiation behavior, on the other hand, is considerably influenced by the finite size of the substrate primarily due to the launching of surface waves and their diffraction at the edge of the substrate. Consequently, the theory of diffraction is occasionally used in conjunction with other methods to improve the prediction of radiation pattern.

The analytical models were the first to be developed for microstrip antennas. They use simplifying assumptions, but generally offer simple and analytical solutions, well suited for an understanding of the physical phenomena and for antenna CAD. In the analytical methods or models, the fields associated with the antenna are divided into an interior region and an exterior region [2], as shown in Figure 2.1.

The interior region is formed by the patch conductor, the portion of the ground plane under the patch, and the walls formed by the projection of the

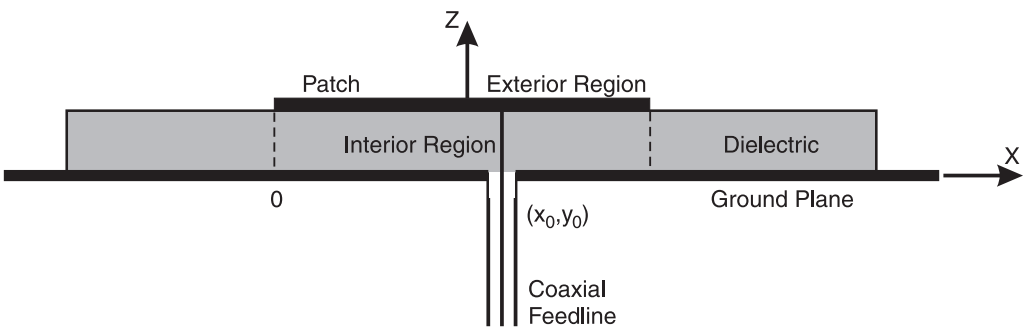

Figure 2.1 Division of fields associated with an antenna into an interior region and an exterior region. (From [2]. © 1979 New Mexico State University. Reprinted with permission.)

patch periphery onto the ground plane. The fields in this region can be modeled as a transmission line section or a cavity giving rise to the designations *transmission line model* and *cavity model*. The exterior region is the rest of the space. This includes the remainder of the ground plane, the remainder of the dielectric, and the top of the patch conducting surface. The fields in the exterior region comprise the radiation field, surface waves, and fringing field. These are characterized in the form of load admittances in some of the models. In simpler models, the effect of these fields is described in the form of increased dielectric loss tangent and equivalent dimensions of the antenna.

Aperture Model for the Fields in the Exterior Region

The mechanism of radiation from a microstrip antenna was described in Section 1.1.2, where it was shown that the radiating edges could be modeled as slots/apertures in the interface plane. The width of the slots in principle should be infinite, but the analysis shows that the electric field decays rapidly away from the edge. In support of this, computed electric and magnetic surface currents on the patch antenna are presented next. Kishk and Shafai carried out such an analysis for a circular patch antenna with finite ground plane [3]. The geometry of the patch is shown in the inset of Figure 2.2. Computed magnetic and electric surface current distributions for the TM_{11} mode are shown in Figures 2.2 and 2.3, respectively. The x axis shows the radial position on the outer boundary of the microstrip surface. Only one-half of the surface contour is shown since the geometry is rotationally symmetric. Points A to B correspond to the position on the ground plane, points B to C represent the dielectric substrate that supports both electric and magnetic surface currents, and points C to D correspond to the patch surface.

The distribution of magnetic current $\overline{M}$, that is, the tangential electric field on the substrate, is shown in Figure 2.2. The magnetic current decreases progressively from C to B, indicating a strong fringing field near C. Figure 2.3 shows that the electric current is strongest on the patch surface and is minimum on the ground plane. The contributions to the radiation field, therefore, are mainly from J_ϕ from the patch and from M_ϕ on the substrate.

Carver and Coffey have plotted dc fringing field distribution near the edge of a microstrip line [2]. They have suggested that a slot width equal to the substrate thickness h with uniform electric field therein can effectively account for the fringing field effect. The length of the apertures is taken to be slightly longer than the physical length of the edge. The increase takes into account the fringing fields at the corners of the patch. For rectangular and circular patches, the width of the aperture can be determined using well-known magnetic wall models. For a rectangular patch, the effective dimensions can be determined from the planar waveguide model of the microstrip (see Appendix

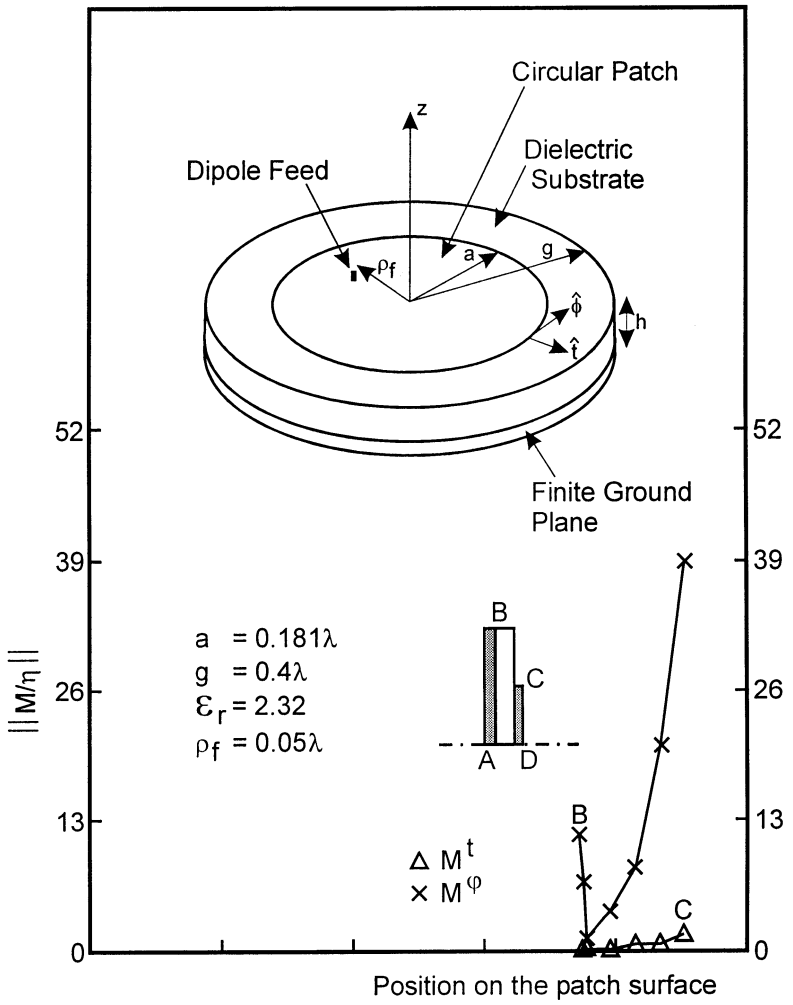

Figure 2.2 Variation of surface magnetic current for the TM_{11} mode of a circular patch. (From [3]. © 1986 IEEE. Reprinted with permission.)

B). For better accuracy, the aperture model has been extended to the nonradiating edges. Therefore, the electric field at the edges of the patch can be modeled as shown in Figure 2.4(a). Extensive calculations show that the outer corners, as modified in Figure 2.4(b), give better agreement with measured antenna characteristics [4]. For ease of implementation, however, most of the analytical models employ the aperture model of Figure 2.4(a). The aperture model is further simplified by assuming that the apertures or slots can be on the ground plane instead of at the interface plane. This approximation does not sacrifice

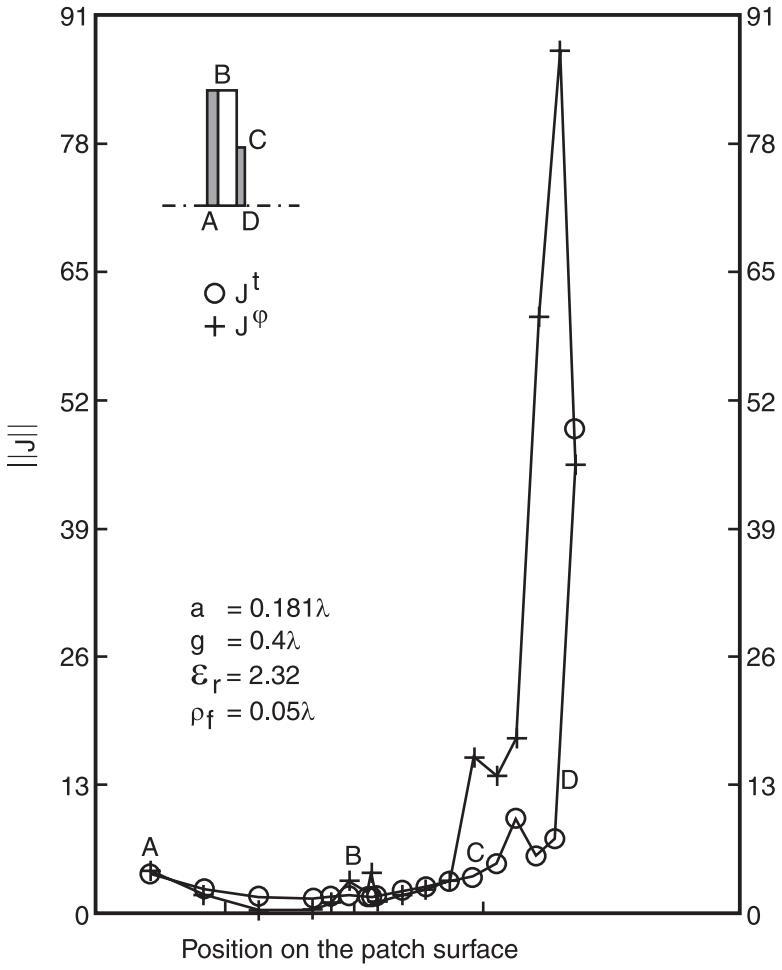

Figure 2.3 Variation of surface electric current for the TM_{11} mode of a circular patch. (From [3]. © 1986 IEEE. Reprinted with permission.)

much of the accuracy if the substrate is thin. The transmission line model based on radiation from apertures is discussed next.

2.2 Transmission Line Model

Rectangular and square patches have a physical shape derived from microstrip transmission lines. Therefore, these antennas can be modeled as sections of transmission lines. Similarly, circular patches, annular rings, and sectors of

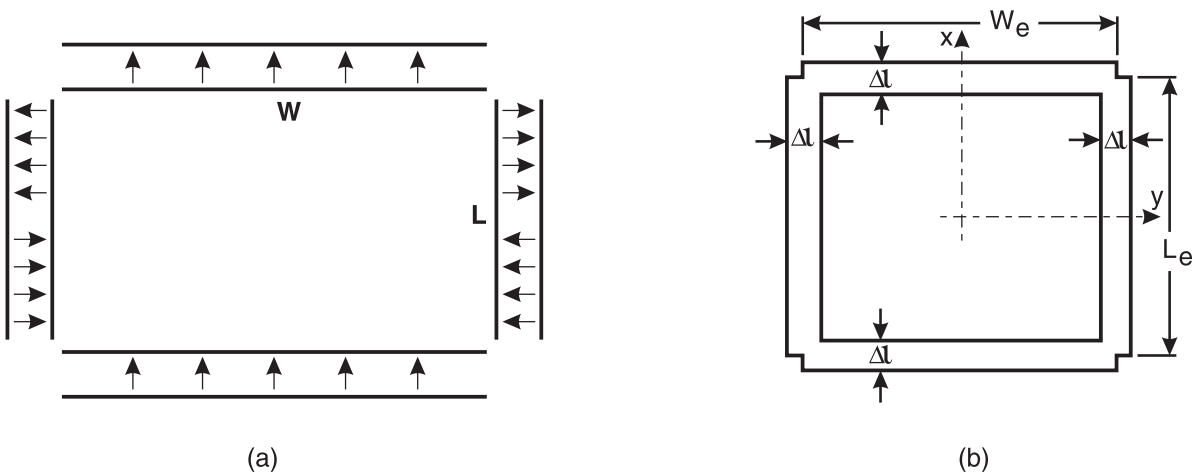

Figure 2.4 Four-slot radiation models: (a) Four-slot model. (b) Four-slot model with corners. (From [1]. © 1992 IEEE. Reprinted with permission.)

circular patches and annular rings can be modeled in terms of sections of radial transmission lines [5–7]. Therefore, the transmission line model is one of the most intuitively appealing models for a microstrip antenna.

2.2.1 Simple Transmission Line Model

This transmission line model [8–10] was the first technique employed to analyze a rectangular microstrip antenna by Munson in 1974 [8]. In this model, the interior region of the patch antenna is modeled as a section of transmission line. The characteristic impedance, Z_0, and propagation constant, β, for the line are determined by the patch size and substrate parameters. Consider a rectangular patch of dimensions $L \times W$ as shown in Figure 2.4. The periphery of this patch is described by four walls/edges at $x = 0, L$ and $y = 0, W$. The four edges of the patch are classified as radiating type or nonradiating type depending on the field variation along their length. The classification is based on the observation that a radiating edge is associated with slow field variations along its length. The nonradiating edge, on the other hand, should have an integral multiple of half-wave variations along the edge, such that there is an almost complete cancellation of the radiated power from the edge. For the TM_{10} mode in the patch, the edges at $x = 0, L$ are radiating types because the electric field is uniform along these edges. The walls at $y = 0, W$ are nonradiating types because of half-wave variation of the field along these edges. The edges at $x = 0, L$ radiate most of the power and are characterized by load admittances $Y_s = G_s + jB_s$. Here, G_s is the conductance associated with the power radiated from the edge or wall, and B_s is the susceptance due to the energy stored in the fringing field near the edge. The effect of the fringing fields at nonradiating edges at $y = 0$ and W is included in the determination of phase constant β. Based on this identification, the equivalent circuit of the rectangular patch antenna is shown in Figure 2.5(a).

The radiation patterns of the patch antenna are assumed to be the same as that of an array of two narrow slots separated by a distance equal to the length of the patch. The input admittance of the antenna at the feed port is obtained by transforming the edge admittances to the feed point. The resulting expression from the equivalent circuit of Figure 2.5(a) is obtained as

$$Y_{\text{in}} = Y_0\left(\frac{Y_0 + jY_s\tan(\beta L_1)}{Y_s + jY_0\tan(\beta L_1)} + \frac{Y_0 + jY_s\tan(\beta L_2)}{Y_s + jY_0\tan(\beta L_2)}\right) + jX_f, \qquad L_1 + L_2 = L \tag{2.1}$$

where $\gamma = j\beta$, Y_0 is the characteristic admittance of the patch fed at $x = L_1$ and X_f is the feed reactance, described in Section 2.9. Derneryd [9, 10]

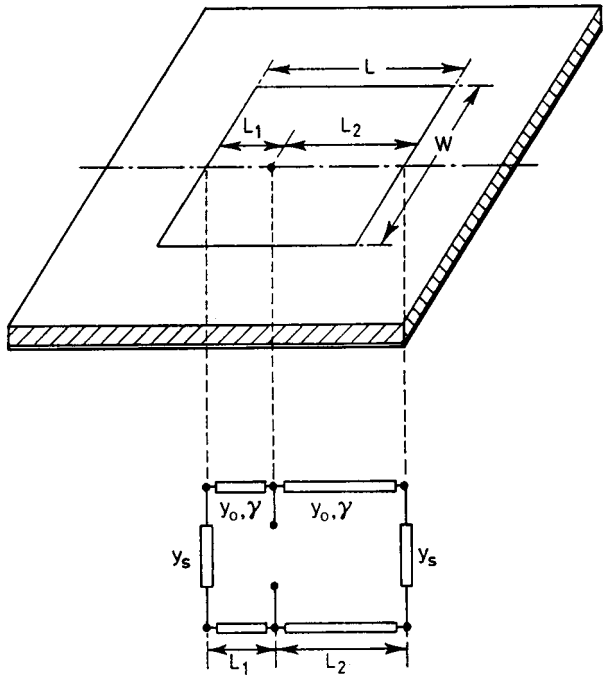

(a)

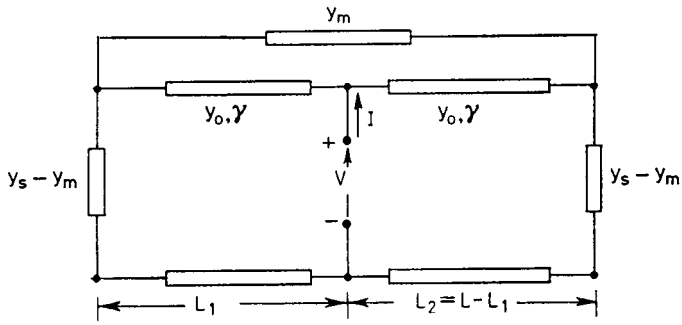

(b)

Figure 2.5 (a) Simple transmission line model and (b) transmission line model with mutual coupling.

introduced some modifications in the simple model. Mutual conductance between the radiating edges was calculated by integrating the interference component of the radiation pattern of two magnetic current sources of the patch antenna. It is given by [10]

$$G_m = \frac{1}{60\pi^2}\int_0^{\pi/2} \sin^2\left(k_0\frac{W}{2}\cos\theta\right)\tan^2\theta\sin\theta J_0(k_0 L\sin\theta)d\theta \qquad (2.2)$$

The edge admittance Y_s is now modified to include G_m, that is, $Y_s = G_s - G_m + jB_s$. This modification provided some improvement in the input impedance of the antenna.

Simplification of (2.1) for the resonant patch, $\beta(L_1 + L_2) \approx \pi$, shows that input resistance at resonance is given by [10]

$$R_{\text{in}} = \frac{1}{2G}\left\{\cos^2(\beta L_1) + \frac{G^2 + B_s^2}{Y_0^2}\sin^2(\beta L_1) - \frac{B_s}{Y_0}\sin(2\beta L_1)\right\} \qquad (2.3)$$

$$\approx \frac{1}{2G}\cos^2(\beta L_1) \quad \text{since } G,\ B_s << Y_0 \qquad (2.4)$$

where $G = G_s - G_m$. The simple model shows that input resistance varies as $\cos^2(\beta L_1)$, and can be used to select the feed position so that impedance match with the source impedance is obtained. In addition to mutual conductance, there is mutual susceptance between the radiating edges. Inclusion of mutual susceptance B_m would give rise to further improvement in input impedance, but in a rectangular patch the two sources are separated such that $\beta L \approx \pi$ and the effect of mutual susceptance on the input resistance may not be much. It is likely to affect the resonant frequency slightly.

In the model discussed above the input impedance of the antenna is not a function of feed position along the y direction. Lier has modified the model due to Derneryd by considering an additional transmission line along the y direction and represented its effect in the form of a reactance [11].

The above transmission line model is conceptually very simple. However, it is very approximate and the model is applicable for a rectangular patch only. The effects of substrate on radiation and input impedance are not considered.

2.2.2 Transmission Line Model With Mutual Coupling

In the improved transmission line model [12], mutual coupling between the radiating edges, is included through a mutual admittance Y_m connected between

the two ends of the transmission line. The feed, microstrip line, or coaxial line, can be represented by an ideal current source at the feed point along the transmission line. The resulting equivalent circuit is shown in Figure 2.5(b). This network can be solved in two different ways for determining the voltage across the feed, and therefore input impedance Z_{in}. In one of the approaches, the mutual admittance is included through voltage-dependent current sources across the self-admittances [12]. This approach requires the equivalent circuit to be a three-port network [see Figure 2.6(a)]. The admittance matrix for this equivalent circuit is obtained as

$$[Y] = \begin{bmatrix} Y_s + Y_0 \coth(\gamma L_1) & -Y_m & -Y_0 \operatorname{csch}(\gamma L_1) \\ -Y_m & Y_s + Y_0 \coth(\gamma L_2) & -Y_0 \operatorname{csch}(\gamma L_2) \\ -Y_0 \operatorname{csch}(\gamma L_1) & -Y_0 \operatorname{csch}(\gamma L_2) & Y_0 (\coth(\gamma L_1) + \coth(\gamma L_2)) \end{bmatrix} \tag{2.5}$$

where $\gamma = \alpha + j\beta$ is the complex propagation constant of the line, α accounting for the dielectric and conductor losses of the antenna. For the feed at port number 3 and feed current I_3, the input admittance obtained from (2.5) (with $I_1 = I_2 = 0$) is [12]

$$\begin{aligned} Y_{\text{in}} &= \frac{I_3}{V_3} \\ &= 2Y_0 \left[\frac{Y_0^2 + Y_s^2 - Y_m^2 + 2Y_0 Y_s \coth(\gamma L) - 2Y_0 Y_m \operatorname{csch}(\gamma L)}{(Y_0^2 - Y_s^2 + Y_m^2)\csc(\gamma L) + (Y_0^2 - Y_s^2 + Y_m^2)\operatorname{csch}(\gamma L)\cosh(2\gamma\Delta) + 2Y_0 Y_s} \right] \end{aligned} \tag{2.6}$$

where

$$\Delta = |L/2 - L_1| = |L_2 - L/2| \tag{2.7}$$

and L_1 and L_2 are defined in Figure 2.5. For an edge-fed microstrip antenna one can use $I_2 = I_3 = 0$, and the input admittance is obtained as [12]

$$Y_{\text{in}} = \frac{Y_0^2 + Y_s^2 - Y_m^2 + 2Y_0 Y_s \coth(\gamma L) - 2Y_0 Y_m \operatorname{csch}(\gamma L)}{Y_s + Y_0 \coth(\gamma L)} \tag{2.8}$$

The effect of aperture blocking by the microstrip feed line should be included in the calculation of Y_s [12].

The above transmission line model has been used in the analysis of a microstrip-fed rectangular patch antenna [12], for the design of a matched

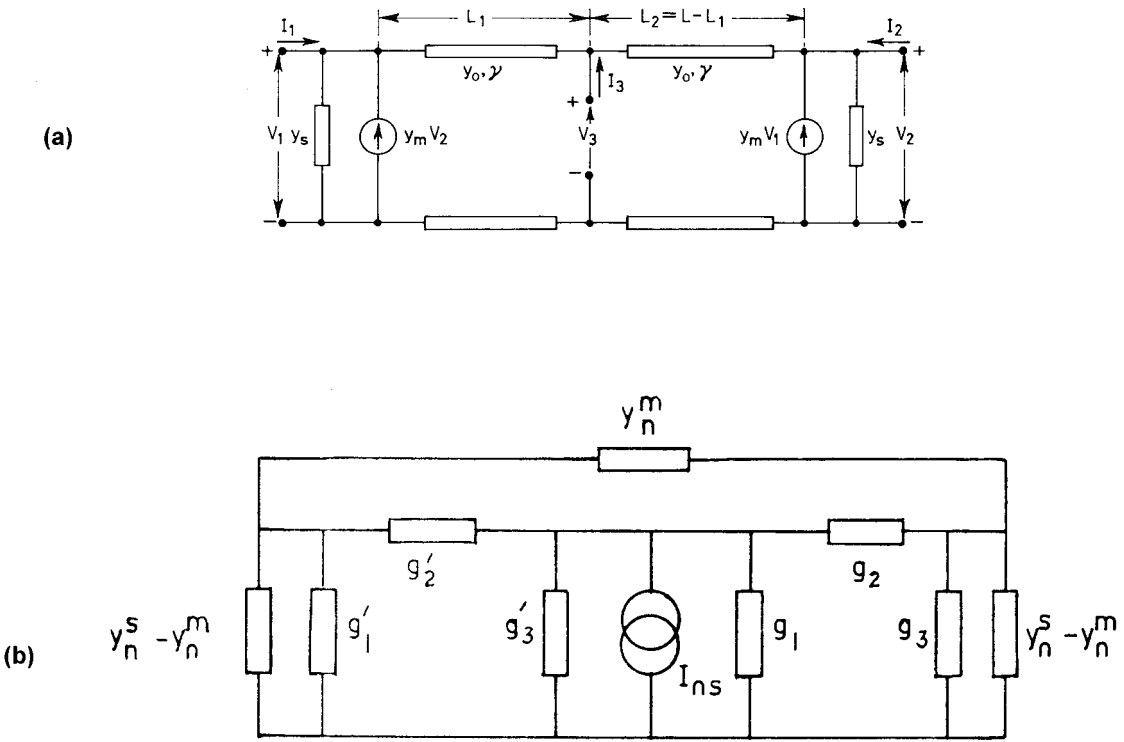

Figure 2.6 (a) Three-port equivalent network for the transmission line model of Figure 2.5(b). (From [12]. © 1984 IEE. Reprinted with permission.) (b) GTLM equivalent network for the transmission line model of Figure 2.5(b). (From [15].)

broadband rectangular patch antenna [4], for the calculation of mutual coupling between rectangular patches [13], and to predict wide-band performance [14]. For mutual coupling analysis, the effect of coupling between the various slots/edges is included by means of voltage-dependent current sources as in the case of a single patch. Because there are four radiating slots (side slots are assumed nonradiating), each slot is characterized by a self-admittance Y_s and three mutual admittances, the latter being defined in terms of voltage dependent current sources.

The equivalent circuits of Figures 2.5 and 2.6 contain the transmission line parameters Y_0 and γ, self-admittance Y_s, and mutual admittance Y_m. The line parameters are defined in Appendix B, and the self- and mutual admittances are described in Sections 2.7 and 2.8, respectively.

The improved transmission line model can be applied to rectangular and square microstrip patches only. Moreover, the variation of fields along the width of the patch is not accounted for. This model can be used for microstrip and coaxial feeds only. Proximity-coupled and aperture-coupled microstrip fed antennas cannot be analyzed. Some of these limitations are overcome in the next model.

2.2.3 Generalized Transmission Line Model

The equivalent circuit of Figure 2.5(b) has been solved differently in an approach called the generalized transmission line model (GTLM) [5, 15, 16]. In this approach, the transmission line sections, which may be nonuniform, on either side of the current source are converted into π-network equivalents. The resulting equivalent circuit is shown in Figure 2.6(b). This equivalent circuit is then simplified using the star-delta and delta-star transformations to obtain the voltage across the current source [6].

The application of GTLM is not restricted to the rectangular patch. Instead it can be applied to any separable geometry of the microstrip antenna. The majority of the practically used patches comes under this category. The patch shapes studied using this model include rectangular patch [15, 16], circular patch [5], circular ring [6], annular and circular sectors [7], and concentric array of circular rings [17] for linear polarization. Elliptical ring [18] and circular ring with a stub [19] have been studied as circularly polarized antennas.

The major difference between the transmission line model and GTLM is that a patch in GTLM is modeled in the form of transmission lines in orthogonal directions. Consequently, variation of fields along the transverse direction is included in GTLM. For application to nonrectangular geometries, the transmission lines are generally nonuniform in nature. Also, the definition

of wall admittance in GTLM is different from that employed in other models. The theoretical background of GTLM is described in detail in Appendix 2A at the end of this chapter. Next we apply this technique to a circular ring microstrip antenna.

Application of GTLM to a Circular Ring Microstrip Antenna

The geometry of a circular ring is shown in Figure 2.7. The separability criteria, (2A.6) of Appendix 2A, is satisfied for a circular geometry. The GTLM can, therefore, be employed to determine the characteristics of a circular ring microstrip antenna [6]. The other transmission line models [8–12], on the other hand, are not applicable for circular geometries. The scale factors in the cylindrical coordinate system are: $h_1 = 1, h_2 = u = \rho$; and the variables u-v are represented by ρ-ϕ. The general solutions for u dependence of E_z are

$$x_1(u) = J_n(ku) = J_n(k\rho),\ x_2(u) = Y_n(ku) = Y_n(k\rho) \tag{2.9}$$

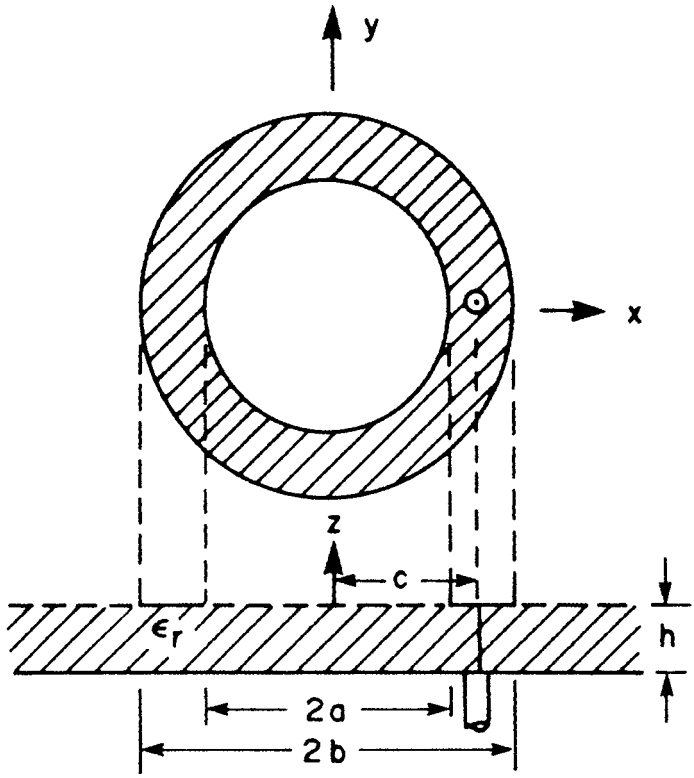

Figure 2.7 Geometry of a circular ring microstrip antenna.

where $J_n(\cdot)$ and $Y_n(\cdot)$ are the Bessel and Neumann functions, respectively, of order n, and k is the wave number in the substrate medium. The v dependence ($v = \phi$) of the field E_z is

$$f_2(v) = \cos n\phi \tag{2.10}$$

Using (2A.27), (2A.28), and (2A.29) of Appendix 2A, the lumped elements of the circuit in Figure 2.6(b) are obtained. These are given by (in the region $c < \rho < b$):

$$g_1 = Y_{11} + Y_{12} = \frac{-j}{\omega\mu\Delta(b, c)}[kb\Delta_1(b, c) + 2/\pi] \tag{2.11}$$

$$g_2 = -Y_{12} = \frac{-2j}{\pi\omega\mu\Delta(c, b)} \tag{2.12}$$

$$g_3 = Y_{22} + Y_{12} = \frac{j}{\omega\mu\Delta(c, b)}[kc\Delta_1(c, b) + 2/\pi] \tag{2.13}$$

with

$$\Delta(b, c) = J_n(kb)Y_n(kc) - Y_n(kb)J_n(kc) \tag{2.14a}$$

and

$$\Delta_1(b, c) = J_n'(kb)Y_n(kc) - Y_n'(kb)J_n(kc) \tag{2.14b}$$

where a prime indicates a derivative with respect to the argument. Expressions for the lumped elements in the region $a < \rho < c$ can be obtained by replacing c with a and b with c in (2.11), (2.12), and (2.13). The expression for mutual wall admittance is derived as [16, 20]

$$y_{12}^m = \frac{jabh}{2\pi\omega\mu}\int_0^{2\pi}\cos\alpha\,\frac{e^{-jk_0r}}{r^3}\Bigg[2(1 + jk_0r)\cos\alpha + \frac{(b\cos\alpha - a)(b - a\cos\alpha)}{r^2}(k_0^2r^2 - 3jk_0r - 3)\Bigg]d\alpha \tag{2.15}$$

with

$$r^2 = a^2 + b^2 - 2ab\cos\alpha$$

The self-conductance can be obtained from (2.15) by setting $b = a$ and retaining the real part. The self-susceptance should be obtained from the equivalent extension formula for the circular ring [21]. *We should point out that the definition of wall admittance in this model is different from the definitions used in other models.*

The equivalent network of Figure 2.6(b) was simplified in [6] using the delta-to-star and star-to-delta transformations and the input impedance was obtained. Computed results for the input impedance for the TM_{12} mode are plotted against frequency in Figure 2.8. Also given in this figure are the measured values. The agreement between the computed and measured results is good. In calculating the total input reactance, the reactances for the neighboring modes (TM_{02} and TM_{51}) are also added to that of the TM_{12} mode. The input resistance, however, was estimated from the TM_{12} mode alone [6]. The accuracy of GTLM can be improved by including the effect of substrate parameters on G_s and y^m_{12} [15].

The GTLM can be applied to a host of separable geometries, some of which are shown in Figure 2.9 [5]. Application of GTLM to an arbitrary patch shape is not possible. Also, some of the feeding techniques such as proximity-coupled and aperture-coupled microstrip feeds cannot be modeled. The stacked patch using GTLM has not been analyzed.

2.2.4 Lossy Transmission Line Model

Another variation of the transmission line model has been suggested by Dubost and coworkers [22–26]. A TEM mode approximation along the symmetry axis

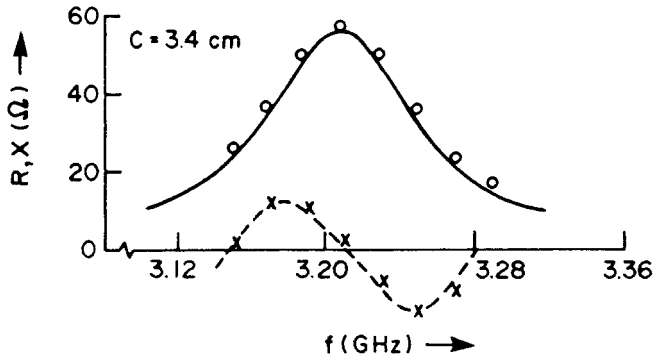

Figure 2.8 Input impedance of a circular ring microstrip antenna seen by a coaxial feed near the TM_{12} mode (a = 3 cm, b = 6 cm, c = 3.4 cm, ϵ_r = 2.2); _____, R computed; - - - -, X computed; ooo, R measured; xxx, X measured. (From [6]. © 1985 IEEE. Reprinted with permission.)

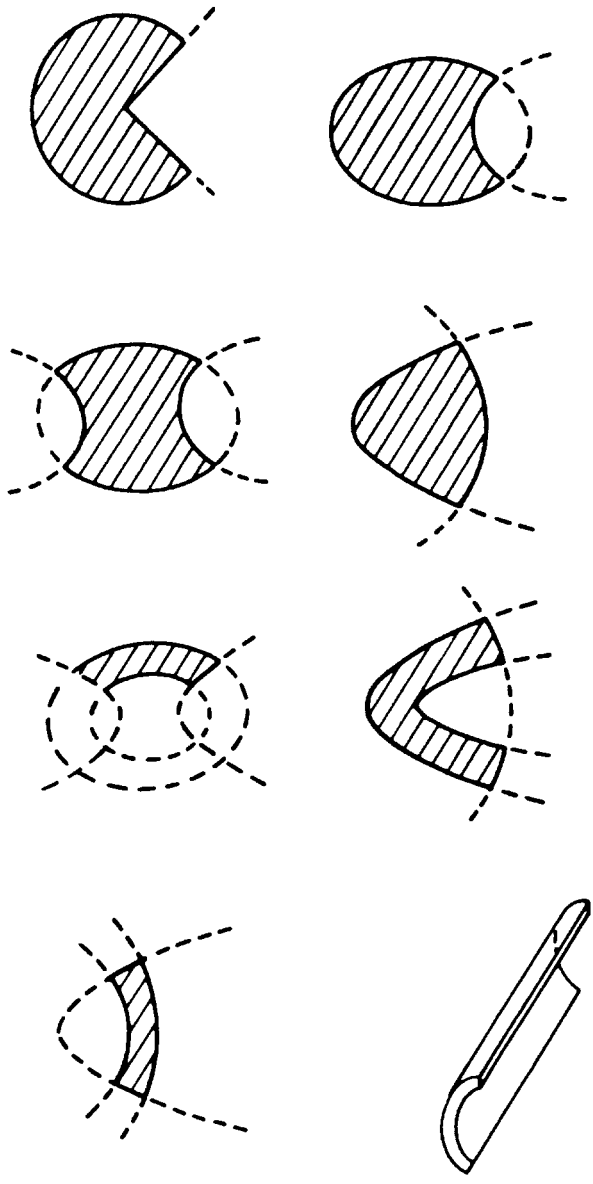

Figure 2.9 Some microstrip patch configurations that can be analyzed using GTLM. (From [5]. © 1985 IEE. Reprinted with permission.)

of the patch is assumed. In this model, various losses such as radiation loss, dielectric loss, and copper loss are combined and assumed distributed along the length of the transmission line in the form of increased dielectric loss. The transmission line section, which may be nonuniform for application to nonrectangular shapes, is divided into a number of small-sized sections. Each section with a particular strip width is characterized by the effective dielectric constant and characteristic impedance. The radiation admittance as a function of strip width is obtained from the solution of the Ricatti equation, which results from the constraint that power delivered to the lossy transmission line equals the power radiated. An analytical or numerical solution for a set of N cascaded sections is obtained to yield input admittance. This model has been applied to a number of geometries including rectangular patch, circular patch, stacked antenna geometry [23, 24], microstrip fed radiating slot, and folded dipoles [25, 26].

The accuracy of transmission line models can be improved by taking into account the effect of surface wave power loss. This may be achieved by including the surface wave conductance in the loads. The effect of multilayered substrate can be incorporated through the effective dielectric constant. Because of the *add-on* approach adopted for including the effects of radiated power, fringing field, and mutual coupling, these models suffer from limited accuracy in the resonant frequency and input impedance for substrates that are not very thin [27]. Extension of this model to large arrays may make the equivalent circuit unwieldy.

The cavity model described next is an improvement over the transmission line model in the sense that the variation of the field along the transverse direction is accounted for.

2.3 Cavity Model

Microstrip patch antennas are narrow-band resonant antennas. They can be termed *lossy cavities*. Therefore, the cavity model [28] becomes a natural choice to analyze patch antennas. A cavity model was advanced by Lo et al. [28–30]. In this model, the interior region of the patch is modeled as a cavity bounded by electric walls on the top and bottom, and a magnetic wall all along the periphery. The bases for this assumption are the following observations for thin substrates ($h << \lambda_0$):

- The fields in the interior region do not vary with z (that is, $\partial/\partial z \equiv 0$) because the substrate is very thin, $h << \lambda_0$.

- The electric field is z directed only, and the magnetic field has only the transverse components in the region bounded by the patch metalization and the ground plane. This observation provides for the electric walls at the top and bottom.
- The electric current in the patch has no component normal to the edge of the patch metalization, which implies that the tangential component of $\overline{H}$ along the edge is negligible, and a magnetic wall can be placed along the periphery. Mathematically, $\partial E_z/\partial n = 0$.

The field distribution in the patch can be divided into two regions: the interior fields and the exterior fields. The interior fields are determined next.

Consider the interior region of the cavity, as shown in Figure 2.1. Since the dielectric is thin, the field distribution in the interior region can be described by TM to z modes with $\partial/\partial z \equiv 0$. As a result, there are only three components of fields E_z, H_x, and H_y. The interior electric field $\overline{E}^i$ must satisfy the inhomogeneous wave equation

$$\nabla \times \nabla \times \overline{E}^i - k^2 \overline{E}^i = -j\omega\mu_0 \overline{J} \tag{2.16}$$

or

$$\nabla_t^2 E_z + k^2 E_z = j\omega\mu_0 \hat{z} \cdot \overline{J} \tag{2.17}$$

where $k^2 = \omega^2 \mu_0 \epsilon_0 \epsilon_r$, $\overline{J}$ is the excitation electric current density either due to the coaxial feed or the microstrip feed, $\hat{z}$ is a unit vector normal to the plane of the patch, and ∇_t is the transverse del operator with respect to the z axis.

In addition to satisfying the wave equation (2.16), the fields must also satisfy the following boundary conditions:

$$\hat{n} \times \overline{E}^i = 0 \quad \text{on the top and bottom conductors} \tag{2.18}$$

$$\left.\begin{aligned} \hat{n} \times \overline{E}^i &= \hat{n} \times \overline{E}^e \\ \hat{n} \times \overline{H}^i &= \hat{n} \times \overline{H}^e \end{aligned}\right\} \quad \text{on the walls} \tag{2.19}$$

Here $\hat{n}$ is the unit outward normal to the walls, $\overline{E}^e$ and $\overline{H}^e$ are the fields in the exterior region.

The fields on the walls, required to enforce (2.19), depend on the substrate parameters ϵ_r and h, the patch configuration and the size of the ground plane,

respectively. It is very difficult to determine these fields accurately even for the simplest patch shape. One of the assumptions that appears to work very well for almost all patch shapes is to assume a magnetic wall all around the periphery of the patch. The magnetic wall is placed at a distance Δ away from the edges of the patch (see Figure 2.10). The outward extension Δ takes into account the energy stored in the fringing fields. It is similar in nature to the effective width of a microstrip line (see Appendix B). Although for simple patch shapes Δ has been found to be a function of substrate parameters and patch shape, it is found to be approximately equal to h, the substrate thickness, for thin low dielectric constant substrates used in microstrip antennas. Equivalent dimensions for well-known antennas are given in Appendix 2B at the end of this chapter.

Under the magnetic wall assumption, (2.19) reduces to

$$\hat{n} \times \overline{H} = 0 \quad \text{on the magnetic walls} \tag{2.20}$$

It is now easy to determine the interior fields. However, these fields are correct only to the first order because the loading effect produced by the exterior fields has not been included in the determination of interior fields. The interior electric field distribution is now obtained in terms of eigenfunctions of the cavity.

The electric field in the patch cavity can be written as

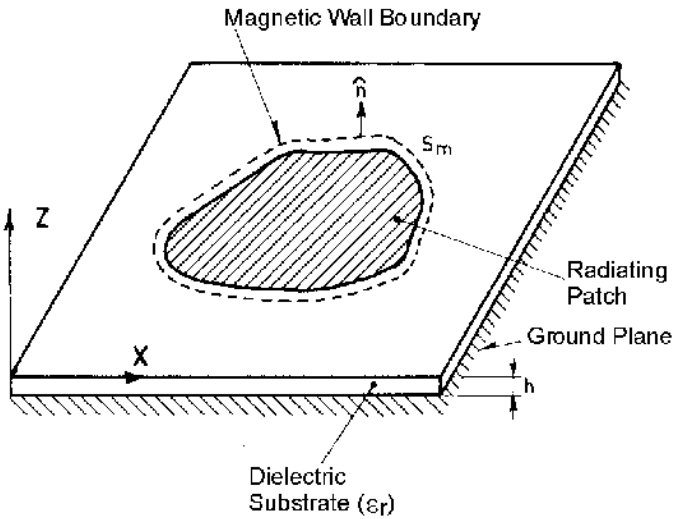

Figure 2.10 Magnetic wall model of a microstrip patch antenna.

$$E_z(x, y) = \sum_m \sum_n A_{mn} \psi_{mn}(x, y) \tag{2.21}$$

where A_{mn} are the amplitude coefficients corresponding to the electric field mode vectors or eigenfunctions ψ_{mn}. The eigenfunctions are solutions of

$$(\nabla_t^2 + k_{mn}^2)\psi_{mn} = 0 \tag{2.22}$$

with

$$\frac{\partial \psi_{mn}}{\partial n} = 0 \quad \text{on the magnetic walls} \tag{2.23}$$

Note here that the eigenfunctions depend on the shape and size of patch metalization, and not on substrate parameters.

Now substitute (2.21) for E_z in (2.17), multiply both sides by ψ_{mn}^* and integrate over the area of the patch. The amplitude coefficients are obtained as

$$A_{mn} = \frac{j\omega\mu_0}{k^2 - k_{mn}^2} \frac{\iint J_z \psi_{mn}^* ds}{\iint \psi_{mn} \psi_{mn}^* ds} \tag{2.24}$$

Therefore,

$$E_z = j\omega\mu_0 \sum_m \sum_n \frac{1}{k^2 - k_{mn}^2} \frac{\iint J_z \psi_{mn}^* ds}{\iint \psi_{mn} \psi_{mn}^* ds} \psi_{mn} \tag{2.25}$$

and

$$\vec{H} = \frac{1}{j\omega\mu_o} \hat{z} \times \nabla E_z \tag{2.26}$$

Alternatively, Green's function for the geometry can be employed to determine the electric field under the patch metalization. The solution for E_z then becomes

$$E_z = \iint G(s|s')J_z ds' \tag{2.27}$$

The interior fields are now used to determine the input impedance of the antenna. Input impedance, in the cavity model, is defined as

$$Z_{\text{in}} = \frac{V_{\text{in}}}{I_{\text{in}}} \tag{2.28}$$

where V_{in} is the RF voltage at the feed point, and is calculated as

$$V_{\text{in}} = -E_z \text{ (at the feed point)}h \tag{2.29}$$

and the feed current

$$I_{\text{in}} = \iint J_z ds \tag{2.30}$$

The preceding procedure will yield the input impedance as purely reactive because all the quantities under the summation sign in (2.25) are real. The effect of radiation and other losses on the input impedance can be included either in the form of an artificially increased substrate loss tangent [28–30] or by an impedance boundary condition at the radiating walls [2, 31]. We describe the first approach here. The other approach is used in the multiport network model described in Section 2.5.

In the cavity model, various types of losses, such as dielectric loss, conductor loss, and radiation loss, are taken into account by defining an effective loss tangent as

$$\delta_{\text{eff}} = I/Q \tag{2.31}$$

where the Q factor of the lossy cavity is defined as

$$Q = \frac{\omega_r W_T}{P_d + P_c + P_r} \tag{2.32}$$

Therefore,

$$\delta_{\text{eff}} = \frac{P_d + P_c + P_r}{\omega_r W_T} \tag{2.33}$$

Here, P_d is the power lost in the imperfect dielectric, P_c is the power lost in the imperfect conductors, and P_r is the power radiated by the antenna. Surface wave loss can be neglected for thin substrates; otherwise, the surface power loss should also be included in (2.33). W_T is the total energy stored in the patch at resonance ω_r. The energy stored is determined by the fields under the patch, and is expressed as

$$W_T = W_e + 2W_m = \frac{\epsilon_0 \epsilon_r}{2} \int\int\int |E_z|^2 dV \tag{2.34}$$

The dielectric loss is calculated from the electric field under the patch,

$$P_d = \frac{\omega \epsilon_o \epsilon_r \tan\delta}{2} \int\int\int |E_z|^2 dV = \omega \cdot \tan\delta \cdot W_T \tag{2.35}$$

where $\tan\delta$ is the loss tangent of the dielectric. The conductor loss P_c is calculated from the magnetic field on the patch metalization and ground plane,

$$P_c = 2\frac{R_s}{2} \int\int |H_s|^2 ds \approx \frac{\omega W_T}{h\sqrt{\pi f \mu_0 \sigma}} \tag{2.36}$$

where R_s is the surface resistivity of the conductors given by $\sqrt{\pi f \mu_0 \sigma}$ and σ is the conductivity of the conductor. The power radiated from the patch P_r can be determined by integrating the radiation field over the hemisphere above the patch, that is,

$$P_r = \frac{1}{2\eta_0} \int_0^{2\pi} \int_0^{\pi/2} (|E_\theta|^2 + |E_\phi|^2) r^2 \sin\theta d\theta d\phi \tag{2.37}$$

The expressions for E_θ and E_ϕ are, in general, very complicated functions of θ and ϕ and substrate parameters. Therefore, a numerical integration is performed.

Alternatively, δ_{eff} can be described in terms of various quality factors. Defining,

$$\text{Dielectric } Q;\ Q_d = \frac{\omega_r W_T}{P_d}$$
$$= 1/\tan\delta \quad \text{from (2.34) and (2.35)} \tag{2.38a}$$

$$\text{Conductor } Q;\ Q_c = \frac{\omega_r W_T}{P_c}$$
$$= h\sqrt{\pi f \mu_0 \sigma} \quad \text{from (2.36)}$$
$$= h/\Delta \ (\Delta \text{ is the skin depth for the conductor}) \qquad (2.38b)$$

$$\text{Radiation } Q;\ Q_r = \frac{\omega_r W_T}{P_r} \qquad (2.38c)$$

one obtains total Q, Q_T, as

$$\frac{1}{Q_T} = \frac{P_d + P_c + P_r}{\omega_r W_T} = \frac{1}{Q_d} + \frac{1}{Q_c} + \frac{1}{Q_r} \qquad (2.39)$$

Use of (2.38) in (2.33) gives the following expression for δ_{eff}:

$$\delta_{\text{eff}} = \tan\delta + \frac{\Delta}{h} + \frac{P_r}{\omega_r W_T} \qquad (2.40)$$

With the losses described in terms of δ_{eff}, the expression for k^2 in (2.25) is now modified as

$$k^2 = k_0^2 \epsilon_r (1 - j\delta_{\text{eff}}) \qquad (2.41)$$

to yield the following expression for E_z:

$$E_z = j\omega\mu_0 \sum_m \sum_n \frac{1}{k_0^2 \epsilon_r (1 - j\delta_{\text{eff}}) - k_{mn}^2} \frac{\iint J_z \psi_{mn}^* \, ds}{\iint \psi_{mn} \psi_{mn}^* \, ds} \psi_{mn} \qquad (2.42)$$

By varying the frequency, the input impedance is calculated at and near the resonant frequency using (2.42) and (2.28). Resonance is indicated by a real input impedance.

The cavity model, as described above, has been applied to a number of patch shapes, including rectangular patches [29, 32, 33], circular patches [28, 29, 34, 35], equilateral triangles [36], circular rings [37–39], and annular and circular sectors [39]. Circular polarization can be predicted using the cavity model [4, 29, 30; Chapter 4]. The cavity model has been modified to include the variation of fields along the substrate thickness [40]. Stacked patch antennas [41] have also been analyzed.

The mutual coupling between the apertures is included in an implicit manner in the cavity model. It is included through the power radiated, which essentially accounts for G_m only, and not mutual susceptance B_m. Moreover, the cavity model does not estimate the ratio of aperture fields correctly in microstrip antennas with more than one aperture, since the fields at the apertures are estimated from a standing wave distribution, in which all the points are in phase [7]. In fact, due to power radiation, the field inside the patch will be progressive in nature, and therefore a phase difference between the aperture fields will occur. It is confirmed by the calculations carried out for a circular ring antenna in a later chapter (see Section 5.6.3). Therefore, the cavity model as such is not suitable for array applications. However, the cavity model has been extended to determine the mutual coupling between rectangular patches [42]. For this, the electric field at the radiating edges is replaced by an equivalent magnetic current and the space wave coupling coefficient can be calculated. The cavity model has also been used to analyze an aperture-coupled patch antenna [43, 44]. In this analysis, the aperture is replaced by an equivalent magnetic current on a conductor surface.

The eigenfunctions required for the cavity model analysis of various geometries are given in Appendix 2B at the end of the chapter. The equivalent dimensions are also given there. The details of the cavity model analysis are given in Chapter 4 for the rectangular patch; in Chapter 5 for the disk, semicircular disk, and circular ring; and in Chapter 6 for the triangular patch antenna.

2.4 Generalized Cavity Model

The cavity model has also been generalized to analyze nonseparable geometries [45, 46]. For this purpose, the given geometry is first converted into an equivalent geometry with magnetic walls at the peripheries as shown in Figure 2.10. The outward extension Δ is based on an educated guess. For regular shaped geometries, the equivalent dimensions are given in Appendix 2B. For other geometries, an extension equal to the substrate thickness h appears to work well for thin, low dielectric constant substrates. Next, the geometry with the magnetic wall is segmented into regular geometries for which eigenfunctions are available. The planar circuit approach [47] is then applied to determine the electric and magnetic fields under the patch. The Q of the patch cavity is next calculated using the procedure given for the cavity model. Finally, the input impedance can be obtained from the ratio of the voltage and current at the feed point. This approach has been used to analyze a rectangular ring [48], a cross-shaped patch [49], an H-shaped patch [48], a square ring microstrip

antenna [49], and a two-port circular patch [50]. A summary of this approach is given next.

In the generalized cavity model, the electric field in the patch is determined first by segmenting the given patch shape into a number of regular shapes for which the Green's functions can be determined. The Green's functions for rectangles, circles, triangles, circular sectors, annular rings, and annular sectors are available [51]. For example, segmentation of the cross-shaped patch into three rectangular segments is shown in Figure 2.11(a). Most of the useful practical patch shapes can be decomposed into regular shapes, and the available Green's functions can be used. A completely arbitrary shape with no plane of symmetry, in general, will give higher levels of cross-polarization in the radiation patterns.

Segmentation

It is possible to determine the fields in a separable geometry by expanding the fields in various segments in terms of their natural modes, and then matching fields along the interconnection lengths. Next, the continuous interconnections between the segments are discretized by interconnections only at a finite number of points. A port is associated with each interconnection point. This is shown in Figure 2.11(a) for the cross-shaped geometry. While approximating the continuous interconnections by a finite number of ports, each port width is kept less than or equal to $\lambda/20$ to optimize the discretization error and efficiency. Here, λ denotes the intrinsic wavelength in the patch. The small size of the port width allows the assumption that the current density is uniform over the width of the port.

The individual segments are now treated as multiport planar networks, and the Z matrices for the same are evaluated using the corresponding impedance Green's function. For a rectangular segment it is defined as [51],

$$Z_{ij}^{s} = \frac{1}{W_i W_j} \int_{PW_i} \int_{PW_j} G^{s}(x_i, y_i | x_j, y_j) d_{s_i} d_{s_j} \tag{2.43}$$

where Z_{ij}^{s} is the ijth element of the Z matrix of the segment, W_i, W_j and PW_i, PW_j are the effective and the physical width of the ith and the jth ports, respectively. For ports entirely within the patch metalization, physical widths and effective widths are equal. The Green's function G^{s} is of the following form for the rectangular geometry of dimensions $a \times b$ [51]:

$$G^{s}(x, y | x', y') = \frac{j\omega\mu_o h}{ab} \sum_{m=-\infty}^{\infty} \sum_{n=-\infty}^{\infty} \frac{\psi_{mn}^{s}(x, y)\psi_{mn}^{s*}(x', y')}{k_{mn}^{2} - k^{2}} \tag{2.44}$$

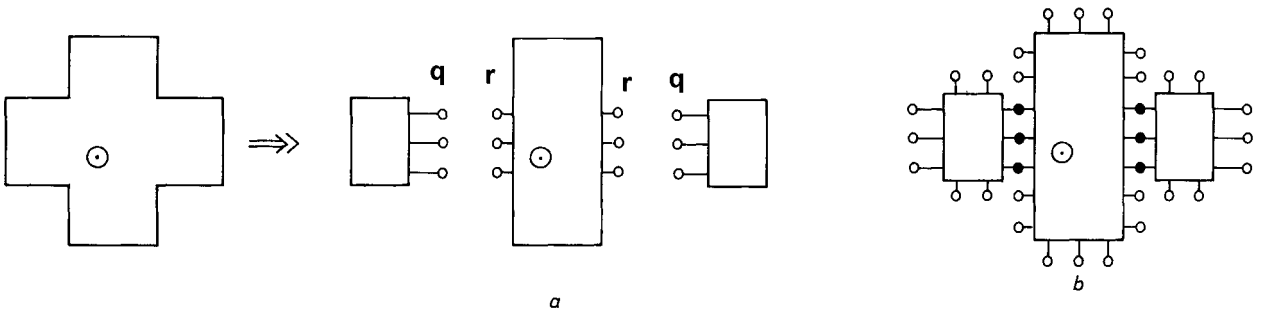

Figure 2.11 (a) Segmentation of a cross-shaped patch into three rectangular segments for the generalized cavity model. (From [49]. © 1986 IEEE. Reprinted with permission.) (b) Multiport network model of the cross-shaped patch antenna. (From [4]. © 1989 Peter Peregrinus. Reprinted with permission.)

Here $\psi^s_{mn}(x, y)$ is the eigenfunction for the mnth mode of the segment, k_{mn} is the corresponding eigenvalue, h is the substrate thickness, and $k^2 = \omega^2 \mu_0 \epsilon_0 \epsilon_r$.

Note that for calculating the impedance matrix of a segment, the local coordinate system can be oriented independent of the coordinate systems chosen for other segments. It should be oriented in such a way that the maximum number of ports lies on the coordinate axis. The integrals in (2.43) are simple and can be obtained in closed form. The input feed is also considered a port (or several ports if the width is more than $\lambda/20$) and can be treated like other port/ports of the segment in the Z-matrix evaluations. For a microstrip feed, the effective width of the feed is used for this purpose.

Multiport Connection Method

The multiport Z matrices for the various segments are now combined by using the multiport connection method [51] to obtain the overall Z matrix of the given structure. For this, the ports of the segments (to be combined) are separated into external (p) ports and connected (c) ports. The connected ports are equally divided into two groups labeled q and r ports such that q ports are the connected ports of one segment and r ports are the corresponding connected ports of the other segment, to be combined [see Figure 2.11(b)]. Based on this labeling, the Z matrix of the combination can now be written as

$$\begin{bmatrix} \vec{V}_p \\ \vec{V}_q \\ \vec{V}_r \end{bmatrix} = \begin{bmatrix} Z_{pp} & Z_{pq} & Z_{pr} \\ Z_{qp} & Z_{qq} & Z_{qr} \\ Z_{rp} & Z_{rq} & Z_{rr} \end{bmatrix} \begin{bmatrix} \vec{i}_p \\ \vec{i}_q \\ \vec{i}_r \end{bmatrix} \tag{2.45}$$

where $\vec{V}_p$, $\vec{V}_q$, $\vec{V}_r$, and $\vec{i}_p$, $\vec{i}_q$, $\vec{i}_r$, are the vectors corresponding to RF port voltages and port currents, respectively, and the Z_{pp} and so on values are the impedance submatrices. Because ports q and ports r are respective ports of two physically separate segments (that are being connected together), submatrices Z_{qr} and Z_{rq} are identically equal to zero. The boundary condition, that is, the continuity of the tangential components of the electric and magnetic fields at the boundary plane between the two combining segments, is expressed in terms of the continuity of port voltages and port currents. These are known as interconnection constraints [51] and are expressed as

$$\vec{V}_q = \vec{V}_r \text{ and } \vec{i}_q + \vec{i}_r = 0 \tag{2.46}$$

Upon substituting (2.46) in (2.45), one obtains the RF currents at the interconnecting q ports $\vec{i}_q$ and the impedance matrix of the combination as

$$\vec{i}_q = [Z_{qq} + Z_{rr}]^{-1}[Z_{rp} - Z_{qp}]\vec{i}_p \tag{2.47a}$$

$$[Z_p] = [Z_{pp}] + [Z_{pq} - Z_{pr}][Z_{qq} + Z_{rr}]^{-1}[Z_{rp} - Z_{qp}] \tag{2.47b}$$

Resonant Frequency

The input impedance evaluated from (2.47b) gives the input reactance of the lossless cavity since the radiation, conductor, dielectric, and surface wave losses have not yet been accounted for. The variation of input reactance with frequency is determined. A very large value of the input reactance indicates resonance because of the antiresonant nature of the patch antenna.

While evaluating the Z matrices of various segments using (2.43), the various combinations of m and n in the evaluation of the Green's function represent the contribution of higher order modes. Because the series is converging, the values of m and n can be limited to $m = M$ and $n = N$, as discussed next. The values of M and N depend on the dimensions of the segment, frequency of operation, and the permittivity of the substrate through k_{MN} and k. They (M and N) should be selected such that the contribution of the $[(M + 1), (N + 1)]$th mode to the Z matrix is insignificant. The values of M and N can be different for different segments depending on their shape and size.

Next, the electric field distribution in the patch is determined. This is required to determine the radiation characteristics and the input impedance.

The electric field E_z^s distribution in terms of the eigenfunctions of the segment is determined in a manner identical to that described in the cavity model (see Section 2.3). The only difference here is that the excitation current lies along the interconnection interfaces of the segment. The details can be found in [46, 51]. The calculation of the electric field in terms of the Green's function of the segment follows.

The excitation current density J_s for a segment is related to the tangential component of the magnetic field on its periphery through the relation $\vec{J}_s = \hat{n} \times \vec{H}$. In the present case, J_s can be determined from the port currents. For this, the current density along the interconnections of the segment is expanded in terms of P modes of the segment. For a rectangular segment, it is given by [46]

$$J_s(s_0) = \frac{-1}{w} \sum_{k=1}^{P} a_k \cos\left\{\frac{(k-1)\pi}{L} s_0\right\} \tag{2.48}$$

where w is the port width, L is the length of the segment along the interconnection, a_k is the expansion coefficient for the kth mode, and s_0 is the running coordinate on the interconnection. The subscript $k = 1$ corresponds to the

TEM mode and P represents the number of modes in the segment that should be taken equal to the number of ports q or r. The coefficients a_k are determined by equating the port current i_k determined in (2.47a) at the kth port to $i(s_0) = wJ_s(s_0)$ evaluated at the middle of kth port, and solving the resultant set of simultaneous equations. Equation (2.48) is repeated for all the interconnections of a segment.

The electric field E_z^s in the segment can be obtained using the definition of Green's function as

$$E_z^s = \frac{1}{h}\sum \int_{S_m} G^s(x, y/s_0) J_s(s_0) ds_0 \tag{2.49}$$

The summation is carried out over all the interconnections of a segment. Use of either eigenfunctions (2.21) or Green's functions (2.49) (both lead to the same result) gives the expression for the electric field distribution in the segment. Similarly, the electric field distribution in other segments can be evaluated. The electric field for the segmented structure is evaluated and plotted at the resonant frequency. From the nature of the variation, the mode of operation can be identified.

Input Impedance

Knowing the electric field distribution at the periphery of the antenna structure, one can calculate the radiation patterns using the magnetic current model described in Section 2.6. From the power radiated and the electric energy stored, the cavity total Q can be evaluated. This is then used to determine the input impedance of the antenna by writing $\delta_{\text{eff}} = 1/Q_T$ as in the cavity model. Then replace k^2 by $k^2{}_0\epsilon_{re}(1 - j\delta_{\text{eff}})$ in the Green's function for a segment to obtain

$$G^s(x, y|x', y') = \frac{j\omega\mu_0 h}{ab} \sum_{m=-\infty}^{\infty} \sum_{n=-\infty}^{\infty} \frac{\psi^s_{mn}(x, y)\psi^{s*}_{mn}(x', y')}{k^2_{mn} - k^2_0\epsilon_{re}(1 - j\delta_{\text{eff}})} \tag{2.50}$$

The Z matrices for the individual segments are again evaluated using the modified Green's function (2.50) and combined as described earlier to give the input impedance of the antenna. By varying the frequency, the input impedance can be evaluated at and near the resonant frequency. It is corrected for feed reactance if a probe feed is used. Resonance is indicated by a real input impedance.

2.5 Multiport Network Model

The multiport network model (MNM) [4] can be considered an extension of the cavity model in which the impedance boundary condition at the periphery is enforced explicitly. This model also takes into account the mutual coupling between various edges. The model makes use of the planar circuit approach [47] and the edge admittances of the patch. Extensive details of MNM are available in [4, Chapter 9]. Below we give a summary of this approach.

In the MNM, the fields in the interior region and the exterior region are modeled separately. The interior region is modeled as a multiport planar circuit, with the ports located all along the periphery, as shown in Figure 2.11(b) for a cross-shaped patch antenna. The fields in the exterior region, which include the fringing fields, radiation fields, and surface wave fields, are represented by the load admittances. Unlike the transmission line model, all of the edges, radiating and nonradiating, qualify to be represented as load admittances in the MNM. Moreover, the load admittance corresponding to a given edge is equally divided into a number of ports. These loads are then connected to the corresponding ports on the planar circuit. Therefore, for a given edge, the number of ports on the multiport network and the load network are identical. The representation of a rectangular patch antenna (fed by a probe current) in the form of a multiport network model is shown in Figure 2.12.

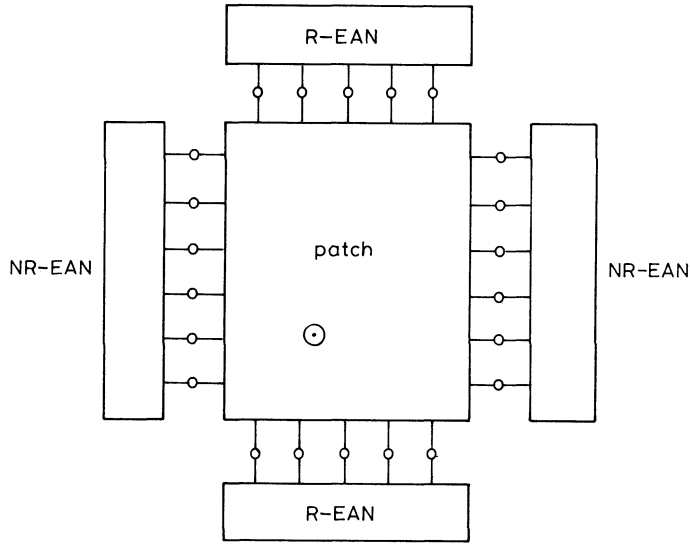

Figure 2.12 Multiport network model, without mutual coupling, of a rectangular patch antenna. (From [4]. © 1989 Peter Peregrinus. Reprinted with permission.)

In the figure, R-EAN stands for the radiating edge admittance network, and NR-EAN denotes the nonradiating edge admittance network. Next, the multiport impedance matrix $[Z^M]$ is obtained using the planar circuit approach, which makes use of the impedance Green's function available for regular/separable geometries [4, 51]. The admittance matrix for the load network $[Y^L]$ can be obtained using the known closed-form expressions for the self-admittance and mutual admittance. The matrices $[Y^M]$ and $[Y^L]$ are now combined in the network analysis [51] to obtain the input impedance of the patch. The matrices $[Z^M]$ and $[Y^L]$ are determined next.

To arrive at the multiport impedance matrix for the planar circuit of the patch, the periphery of the patch is first divided into a number of edges, each of which is then classified as radiating type or nonradiating type. The classification is based on the observation that a radiating edge is associated with slow field variation along its length. The nonradiating edge, on the other hand, should have an integral multiple of half-wave variations along the edge, such that there is almost complete cancellation of the radiated power from the edge. A simple example of this nature of field variation is found in the resonant rectangular patch operated in the TM_{mo} mode or the TM_{on} mode. The edge length is next divided into a number of equal parts, to each of which is assigned a port. The port terminals are located at the middle of the port width, with one terminal on the patch side and the other ground. For the radiating edge, the physical port width W_i is typically chosen to be about $\lambda/10$, while for the nonradiating edge, the port width is decreased to about $\lambda/20$, because of the rapid field variation. Assuming that the port voltages v_i and the port currents I_j are constant over the port widths, the impedance matrix element for $[Z^M]$ is defined as

$$Z_{ij}^M = \frac{1}{W_i W_j} \int_{W_i} \int_{W_j} G(x_i, y_i | x_j, y_j) d_{s_i} d_{s_j} \tag{2.51}$$

where $(x_{i,j}; y_{i,j})$ the values denote the location of the two ports of widths W_i and W_j, respectively. The impedance Green's function G(•|•) for the patches of regular shapes like rectangles, circles, rings, sectors of circles and rings, and three types of triangles are available [4, 51]. These Green's functions usually employ a doubly infinite series with each term representing a particular mode of the planar resonator with magnetic walls along the periphery.

The fields in the exterior region of the patch are represented by a load admittance matrix $[Y^L]$. It is a square matrix of the same size as the multiport matrix $[Z^M]$. Each element of $[Y^L]$ is a complex number, the real part representing the power loss and the imaginary part the energy stored in the fringing

field. The port self-admittances are placed at the diagonal locations in the matrix, while the off-diagonal entries represent the mutual coupling between various ports. The matrix $[Y^L]$ is a diagonal matrix for patches with a single edge. For simplicity, the self terms for the nonradiating edges are taken to be purely imaginary, assuming that the associated power loss is negligible although the surface wave loss may be significant for thicker substrates. The load admittance values are calculated separately for each edge. Then, this edge admittance is divided equally among the various ports constituting the edge. The load at each of the ports on the radiating edge is a parallel combination of G and C, and on the nonradiating edge it is simply the fringing field capacitance C. The edge admittance networks are shown in Figure 2.13.

The MNM of a rectangular patch antenna incorporating the effect of mutual coupling between the radiating edges is shown in Figure 2.14. The patch is fed a nonradiating edge. Here, the mutual coupling effect is described by a separate block labeled MCN (mutual coupling network). Similar MCNs can be included between a nonradiating edge and a radiating edge, and between two nonradiating edges, or between the edges of different patches in an array.

Edge-Admittance Network and Mutual Coupling Network

The edge-admittance networks are shown in Figure 2.13. The values of G and C can be obtained from the closed-form expressions for radiation conductance and fringing field susceptance given in Section 2.7. These expressions can be used straightaway if the voltage distribution along the edge is uniform. However, for a nonuniform distribution of voltage, some correction is needed, as described next.

Let the edge length be W, and the power radiated from it for a uniform voltage distribution be P_r. Then using $P_r = 1/2\, V^2 G_r$, one obtains the radiation conductance per unit length as $2P_r/W$ for $V = 1$V. But when the normalized

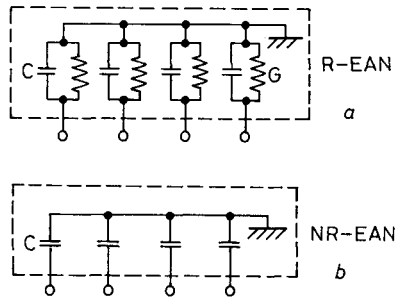

Figure 2.13 Edge admittance networks (EAN) for (a) radiating edge and (b) nonradiating edge. (From [4]. © 1989 Peter Peregrinus. Reprinted with permission.)

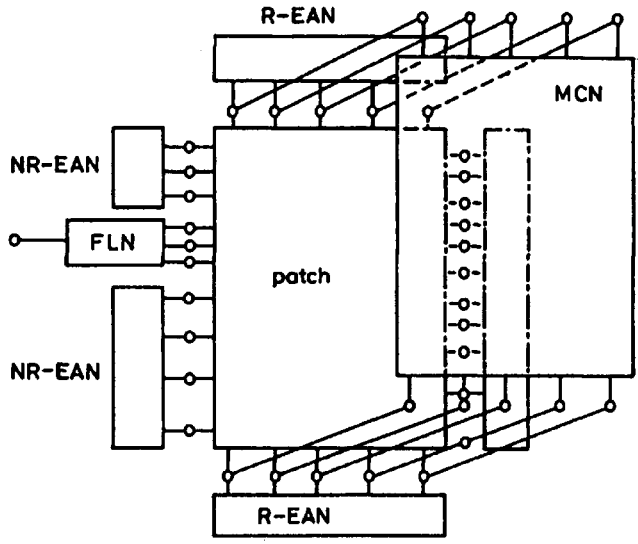

Figure 2.14 Multiport network model of a rectangular patch antenna incorporating mutual coupling between the radiating edges. (From [4]. © 1989 Peter Peregrinus. Reprinted with permission.)

voltage distribution along the edge is $V(s) = f(s)$, the radiation conductance per unit length is obtained as [4, Chapter 9]

$$G_r = \frac{2P_r}{\int_0^W f^2(s)ds} \tag{2.52}$$

where s denotes the position along the radiating edge. If we divide the edge length W into n ports of equal width W/n, the conductance shunting each of the ports is $G_r W/n$. The voltage distribution $f(s)$ for the regular shaped patches is known a priori from their eigenfunctions. However, for nonregular shaped patches and patches with discontinuities, for example, the MNM can be used to determine an accurate $f(s)$ in an iterative fashion. Similar to the radiation conductance, the surface conductance G_s can be expressed as [4, Chapter 9]

$$G_s = \frac{2P_{\text{sur}}}{\int_0^W f^2(s)ds} \tag{2.53}$$

It was pointed out in Chapter 1 that $G_s << G_r$ for thin substrates without any cover layer on the patch. The edge susceptance is also distributed uniformly over the n ports.

The multiport network model has been used to determine mutual coupling between two rectangular patches. For this, the mutual coupling between any two ports is determined by first converting the electric field on one of the ports into the equivalent magnetic current $\overline{M}_i = -\hat{n} \times \overline{E}_i h$, the unit vector $\hat{n}$ is taken normal to the ground plane, and the electric vector $\overline{E}_i$ across a slot over the ground plane. The ground plane can be removed by imaging $\overline{M}_i$ to give the current $2\overline{M}_i$ radiating in free space. Next, the magnetic field $\overline{H}_j$, radiated by the magnetic current $2\overline{M}_i$, is determined at the location of port j. The current density $\overline{J}_j = \hat{n} \times \overline{H}_j$ induced on port j is then calculated. The mutual admittance between the ports i and j is then given by [4, Chapter 9]

$$Y_{ij} = J_j W_j / M_i \tag{2.54}$$

In this way the mutual admittance matrix between two radiating edges and therefore the mutual coupling network (MCN) between two adjacent patches can be determined. The MCN between two patches is shown in Figure 2.15. Here, MCN accounts for coupling between all four radiating edges. Comparison of mutual coupling $|S_{21}|$ based on MNM with the transmission line model and experimental results is shown in Figures 2.16 and 2.17 for the E-plane and H-plane mutual coupling, respectively [52]. The agreement with the experimental values is found to be better for MNM.

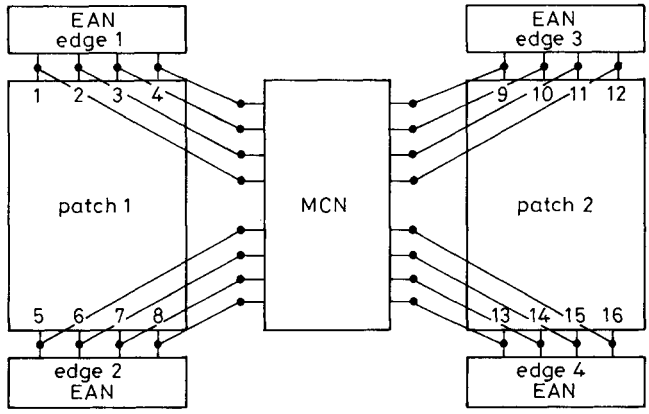

Figure 2.15 A mutual coupling network (MCN) representing the coupling between two adjacent patches in an array. (From [52]. © 1989 IEEE. Reprinted with permission.)

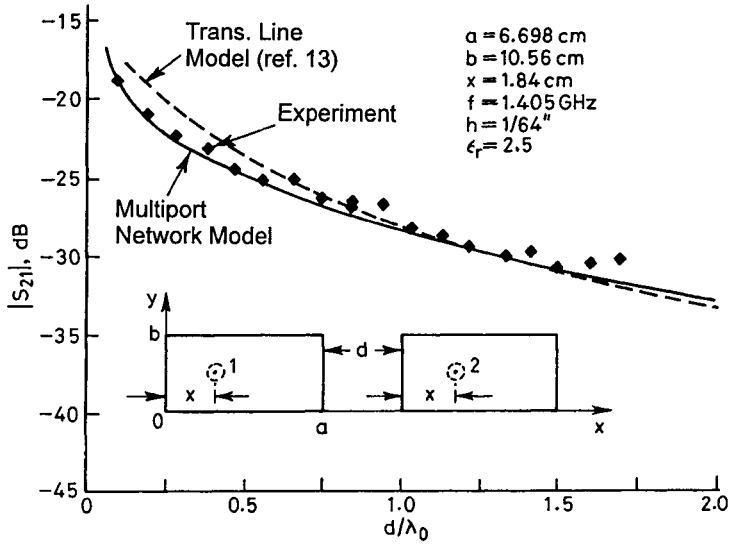

Figure 2.16 Comparison between theoretical and experimental results for E-plane mutual coupling between two rectangular microstrip patches. (From [52]. © 1989 IEEE. Reprinted with permission.)

The MNM has been applied to analyze a variety of microstrip antennas [50, 53–59], including rectangular patches, circular polarization from truncated square patches [55], square patches with diagonal slots [55], pentagonal shaped patches [54], broadband gap-coupled multiresonator rectangular patches [56, 57], direct coupled rectangular patches [58], and two-port rectangular patches [59]. Recently, MNM has been used to model proximity-coupled rectangular microstrip antennas [60]. One of the major advantages of MNM is that any discontinuity in the patch is also included in the analysis. The discontinuity effect is not calculated separately and *added* in the form of a lumped reactance.

2.6 Radiation Fields

The radiation pattern of an antenna is one of the most important characteristics and easiest to determine for patch antennas. The calculation of the radiation patterns from a patch antenna follows the same approach irrespective of the analytical models discussed earlier. It is assumed that the electric field at the perimeter of the patch is known. The equivalent source concept [61] is then used to determine the radiation fields. The equivalent magnetic current is defined as

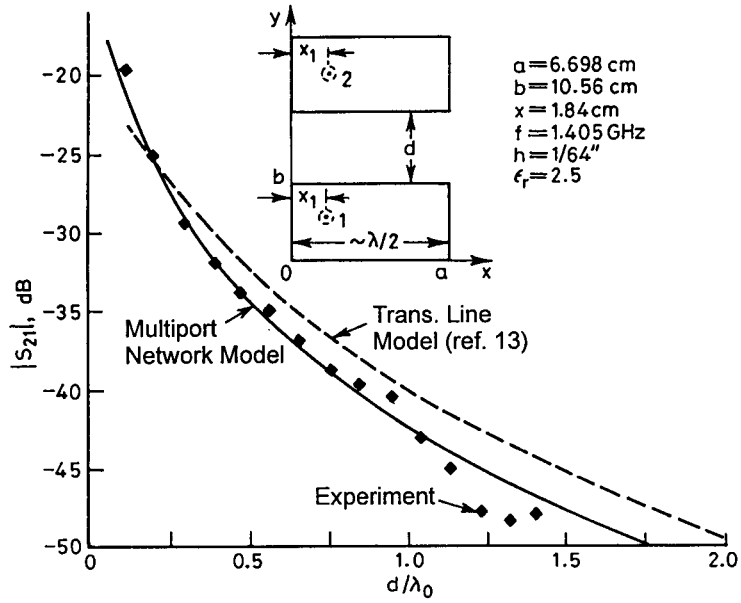

Figure 2.17 Comparison between theoretical and experimental results for H-plane mutual coupling between two rectangular microstrip patches. (From [52]. © 1989 IEEE. Reprinted with permission.)

$$\vec{M} = \vec{E} \times \hat{n} \tag{2.55}$$

If the substrate thickness h is much less than the wavelength λ_0, its effect on the radiation patterns is small and M can be assumed to radiate in free space. One can then use the vector potential approach described in Section 1.5.1 to determine the radiation patterns. Let us consider an aperture of dimensions $h \times W$ with $E_x = -V_0/h$ V/m, and $E_y = 0$. For this case, $M_x = 0$ and

$$M_y = \begin{cases} V_0/h & -\dfrac{W}{2} \le y \le \dfrac{W}{2}, -\dfrac{h}{2} \le x \le \dfrac{h}{2} \\ 0 & \text{elsewhere} \end{cases} \tag{2.56}$$

It has been derived in Chapter 1, (1.29), that

$$E_\theta = -jk_0 V_0 W \frac{e^{-jk_0 r}}{4\pi r} \sin c(k_0 h \sin\theta \cos\phi/2) \sin c(k_0 W \sin\theta \sin\phi/2) \cos\phi \tag{2.57}$$

$$E_\phi = jk_0 V_0 W \frac{e^{-jk_0 r}}{4\pi r} \mathrm{sinc}(k_0 h \sin\theta \cos\phi/2) \mathrm{sinc}(k_0 W \sin\theta \sin\phi/2) \cos\theta \sin\phi \tag{2.58}$$

The effect of the ground plane and substrate on the radiation patterns can be included in a simple manner by imaging the slot at an electrical distance kh from the ground plane, $k = k_0\sqrt{\epsilon_r}$ [31]. This approach results in an array factor $2\cos(kh\cos\theta)$ if the patch lies in the x-y plane. A better and rigorous approach is based on the reciprocity theorem applied to two infinitesimal dipoles, one located on the surface of the substrate and the other in free space at a very large distance away from it [62]. It yields the following factors for the E-plane and H-plane radiation patterns:

$$F_3(\theta) = \frac{2\cos\theta\sqrt{\epsilon_r - \sin^2\theta}}{\sqrt{\epsilon_r - \sin^2\theta} - j\epsilon_r \cos\theta \cot(k_o h\sqrt{\epsilon_r - \sin^2\theta})} \quad \text{for E-plane pattern } (\phi = 0°) \tag{2.59a}$$

and

$$F_4(\theta) = \frac{2\cos\theta}{\cos\theta - j\sqrt{\epsilon_r - \sin^2\theta}\cot(k_o h\sqrt{\epsilon_r - \sin^2\theta})} \quad \text{for H-plane pattern } (\phi = 90°) \tag{2.59b}$$

The radiation patterns for a substrate loaded patch are obtained by multiplying (2.58) and (2.59).

The analysis for the radiation field of a rectangular slot can be used to determine the radiation patterns of a rectangular patch antenna by multiplying the radiation fields of a slot with the array factor (see Chapter 4). Radiation patterns for other microstrip antennas can be similarly derived.

2.7 Aperture Admittance

In the (aperture) models discussed earlier, the effect of fields in the exterior region on the input impedance is represented by a load admittance. The load conductance is associated with the power radiated from the aperture, whereas the load susceptance is due to the energy stored in the near field. The load

conductance or radiation conductance G_r is defined as an ohmic conductance (distributed or lumped), which will dissipate a power equal to that radiated by the aperture. The power radiated and the energy stored can be calculated if the aperture field distribution is known exactly. It is difficult to determine the exact aperture field. However, the ideal open-circuit field behavior is found to give a fairly accurate description of the radiated power. The aperture susceptance is determined from the near-field analysis.

Radiation from an open end of a microstrip line has been determined by many investigators [63–67]. The approaches include current flowing on the conducting surface, and the aperture method. The two formulations are found to be equivalent [68] provided no approximations are made. We discuss the aperture field approach. The details of electric current formulation can be found in [63] and Chapter 3.

2.7.1 Aperture Conductance, G_s

Consider a radiating aperture or slot in the plane of the patch as shown in Figure 2.18. The aperture conductance of this slot has been calculated by a number of authors using different approximations [4, Chapter 10]. The simplest approach is to assume that the field distribution in a finite length slot of width h is similar to that in an infinitely long uniformly excited slot of width h in a ground plane. The admittance per unit length of the slot y_s is then calculated. The admittance for a slot of length W is then given by

$$Y_s = Wy_s \tag{2.60}$$

To determine y_s, the slot is analyzed as a one-dimensional problem with a uniform aperture field distribution

$$\vec{E}_a = \begin{cases} \hat{y}E_0 & \text{for } |y| \le h/2 \\ 0 & \text{elsewhere} \end{cases} \tag{2.61}$$

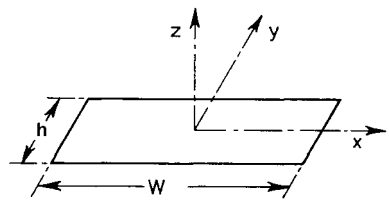

Figure 2.18 An equivalent slot radiator in an infinite, perfectly conducting plane.

The Fourier transform of the aperture field with respect to y is taken to describe the fields in the aperture in terms of plane waves. One obtains

$$\tilde{E}_y(k_y) = E_0 \int_{-h/2}^{h/2} e^{jk_y y} dy = E_0 h \frac{\sin(k_y h/2)}{k_y h/2} \tag{2.62}$$

The complex power radiated per unit slot length $(p + jq)$ is given by [61, Chapter 4]

$$p = \frac{k_o}{4\pi\eta_0} \int_{-k_0}^{+k_0} |\tilde{E}_y|^2 \frac{dk_y}{\sqrt{k_0^2 - k_y^2}} \tag{2.63a}$$

$$q = -\frac{k_0}{4\pi\eta_0} \left(\int_{-\infty}^{-k_0} + \int_{+k_0}^{+\infty} |\tilde{E}_y|^2 \frac{dk_y}{\sqrt{k_y^2 - k_0^2}} \right) \tag{2.63b}$$

where $k_0 = 2\pi/\lambda_0$ and $\eta_0 = 120\pi$. The equivalent aperture admittance corresponding to the radiated power is defined as

$$p + jq = \frac{1}{2} y_s^* |E_0 h|^2 = \frac{1}{2}(g_s - jb_s)|E_0 h|^2 \tag{2.64}$$

Comparison of (2.63) and (2.64) gives

$$g_s = \frac{k_0}{\pi\eta_0} \int_0^{+k_0} \frac{\sin^2(k_y h/2)}{(k_y h/2)^2} \frac{dk_y}{\sqrt{k_0^2 - k_y^2}} \tag{2.65a}$$

$$b_s = \frac{k_0}{\pi\eta_0} \int_{k_0}^{\infty} \frac{\sin^2(k_y h/2)}{(k_y h/2)^2} \frac{dk_y}{\sqrt{k_y^2 - k_0^2}} \tag{2.65b}$$

The integrals in (2.65) can be approximated to yield the following closed-form expressions [4, Chapter 10]:

$$g_s \approx \frac{k_0}{2\eta_0}\left(1 - \frac{s^2}{24}\right) \tag{2.66}$$

$$b_s \approx -\frac{k_0}{\pi\eta_0}\left\{\left(\ln\frac{s}{2} + \gamma - \frac{3}{2}\right)\left(1 - \frac{s^2}{24}\right) + \frac{s^2}{288}\right\} \tag{2.67}$$

where $s = k_0 h$ is the normalized slot width, and $\gamma = 0.577216$. The maximum truncation error in (2.66) and (2.67) is less than 0.1% for $s \leq 1$.

Equation (2.67) gives very approximate values for the aperture susceptance because it is found to be a sensitive function of the field distribution in the aperture, which is governed by the charge density distribution at the metal edge. Therefore, a static analysis of the open-end behavior of the microstrip edge yields more accurate values for the susceptance. We will use closed-form expressions based on the static analysis as well as full-wave analysis.

The next best approximation for the calculation of the aperture admittance is to analyze radiation from a finite length slot of width h in a ground plane as shown in Figure 2.18. Again the electric field distribution is assumed to be uniform along the length and width of the slot, that is,

$$\vec{E}_a = \begin{cases} \hat{y}E_0 & \text{for } |y| \leq h/2,\ |x| \leq W/2 \\ 0 & \text{elsewhere} \end{cases} \tag{2.68}$$

The analysis problem is now a two-dimensional one. Therefore, double Fourier transform of the aperture field is taken to give

$$\begin{aligned} \tilde{E}_y &= E_0 \int_{-h/2}^{h/2} \int_{-W/2}^{W/2} e^{jk_x x} dx dy \\ &= E_0 Wh \frac{\sin(k_x W/2)}{k_x W/2} \frac{\sin(k_y h/2)}{k_y h/2} \end{aligned} \tag{2.69}$$

The complex power radiated by the slot in Figure 2.18 is found by integrating the complex Poynting vector over the aperture area. One obtains

$$P + jQ = \frac{1}{2} \iint_{\text{aperture}} (\vec{E}_a \times \vec{H}_a^*) \cdot \hat{z}\, dx dy \tag{2.70}$$

where $\vec{H}_a$ is the aperture magnetic field. Expressed in terms of the Fourier transformed aperture field, (2.70) becomes [4, Chapter 10]

$$P + jQ = \frac{1}{8\pi^2 \eta_0 k_0} \int_{-\infty}^{+\infty} \int_{-\infty}^{+\infty} \left(k_z^2 |\tilde{E}_y|^2 + |k_y \tilde{E}_y|^2 \right) \frac{dk_x dk_y}{k_z^*} \tag{2.71}$$

where

$$k_z = \begin{cases} +\sqrt{k_0^2 - k_x^2 - k_y^2} & \text{for } k_0^2 \geq k_x^2 + k_y^2 \\ -j\sqrt{k_x^2 + k_y^2 - k_0^2} & \text{for } k_0^2 < k_x^2 + k_y^2 \end{cases} \tag{2.72}$$

The radiated power can also be written in terms of network parameters as

$$P + jQ = \frac{1}{2}(G_s - jB_s)|E_0 h|^2 \tag{2.73}$$

Comparison of (2.71) and (2.73) yields the following equation:

$$G_s = \frac{1}{\pi^2 \eta_0 k_0 |E_0 h|^2} \int_0^{k_0} \left\{ \int_0^{\sqrt{k_0^2 - k_x^2}} |\tilde{E}_y|^2 (k_0^2 - k_x^2) \frac{dk_y}{\sqrt{k_0^2 - k_x^2 - k_y^2}} \right\} dk_x \tag{2.74}$$

Use of (2.69) for $\tilde{E}_y$ in (2.74) gives

$$G_s = \frac{4}{\pi^2 \eta_0 k_0} \int_0^{k_0} \frac{k_0^2 - k_x^2}{k_x^2} \sin^2(k_x W/2) \times \left\{ \int_0^{\sqrt{k_0^2 - k_x^2}} \frac{\sin^2(k_y h/2)}{(k_y h/2)^2} \frac{dk_y}{\sqrt{k_0^2 - k_x^2 - k_y^2}} \right\} dk_x \tag{2.75}$$

The inner integral of (2.75) can be expressed as a double integral of $J_0(\cdot)$. Expanding the Bessel function in a Maclaurin's series, carrying out the integration term by term, and retaining only the first two terms of the series gives [4, Chapter 10]

$$G_s \approx \frac{1}{\pi\eta_0}\left\{\left(wSi(w) + \frac{\sin w}{w} + \cos w - 2\right)\left(1 - \frac{s^2}{24}\right) + \frac{s^2}{12}\left(\frac{1}{3} + \frac{\cos w}{w^2} - \frac{\sin w}{w^3}\right)\right\} \tag{2.76}$$

where $w = k_0 W$, $s = k_0 h$, and

$$Si(x) = \int_0^x \frac{\sin u}{u}\, du$$

In a simpler approach for radiation conductance, the radiation fields due to a slot of length W are calculated. Integration of the radiation fields yields the power radiated. Use of (2.73) then gives the value of the radiation conductance. Approximations in the integration yield the following expression [63]:

$$G_s = \begin{cases} W^2/(90\lambda_0^2) & \text{for } W \le 0.35\lambda_0 \\ W/(120\lambda_0) - 1/(60\pi^2) & \text{for } 0.35\lambda_0 \le W \le 2\lambda_0 \\ W/(120\lambda_0) & \text{for } 2\lambda_0 < W \end{cases} \tag{2.77}$$

Another approach is based on the Wiener-Hopf technique [69, 70]. It is applicable to an infinitely long microstrip edge, but the effect of substrate dielectric constant is included in the analysis. A closed-form expression due to Gogoi and Gupta [69] is given:

$$G_s = W\frac{7.75 + 2.2k_0h + 4.8(k_0h)^2}{1000\lambda_0}\left\{1 + \frac{(\epsilon_r - 2.45)(k_0h)^3}{1.3}\right\} \tag{2.78}$$

The accuracy of (2.78) is 1.1% for $0.05 \le k_0 h \le 0.6$ and $2.45 < \epsilon_r < 2.65$. Bhattacharyya and Garg [71] have analyzed radiation from a rectangular slot on a grounded dielectric substrate. The analysis, as before, is carried out in the spectral domain. However, a closed-form expression is not available. The effect of substrate on the radiation conductance is plotted in Figure 2.19 [15]. The length of the slot is 10.6 cm and the width is taken to be equal to the substrate thickness. It is observed from here that the radiation conductance decreases with an increase in the dielectric constant of the substrate.

The values of G_s obtained from (2.76), (2.77), and (2.78) have been compared in [4, Chapter 9]. It is found that (2.76) and (2.77) compare very

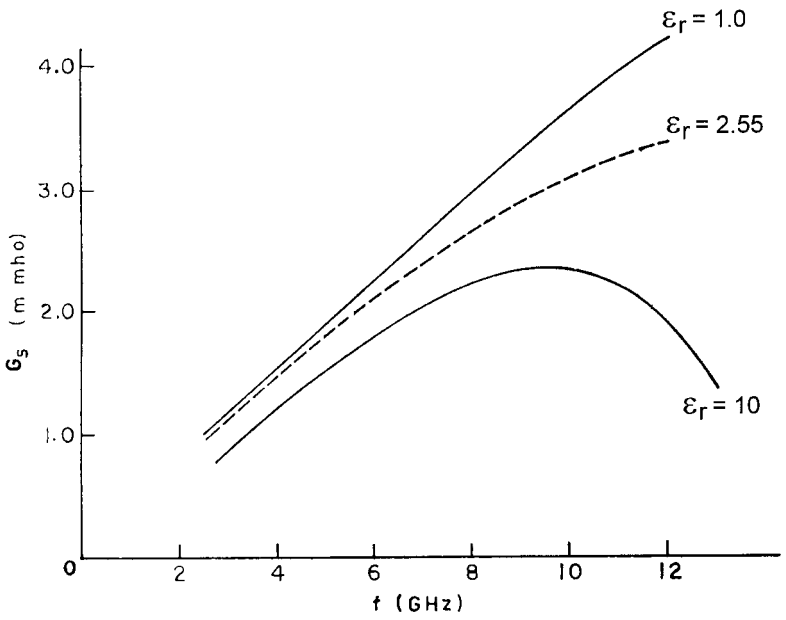

Figure 2.19 Radiation conductance G_s for a slot on a grounded substrate, $W = 10.6$ cm, $h = 0.159$ cm. (From [15]. © 1985 Indian Institute of Technology. Reprinted with permission.)

well for $W/\lambda_0 \leq 2$, whereas (2.77) and (2.78) agree for $W/\lambda_0 \geq 2$. Therefore, it is recommended that (2.77) be used for G_s for thin substrates with $h/\lambda_0 \leq 0.02$.

There is a need for improvement in the expression for G_s. This should include the effect of ϵ_r and should be valid for thicker substrates also.

2.7.2 Edge Susceptance, B_s

Full-wave analysis of the assumed aperture field does not give accurate results for the aperture susceptance. For this we invoke the idea of open-end effect to model the susceptance of a radiating edge. Both quasi-static as well as full-wave analyses have been reported.

One of the formulas for B_s is based on the concept of the edge effect in a microstrip line [72]. The rectangular patch of dimensions $L \times W$ has four edges at $x = 0$, L and $y = 0$, W. To determine the end capacitances at the $y = 0$ and $y = W$ planes, the patch is modeled as a microstrip line of width L and length W_e. The capacitance of this line can be calculated from the characteristic impedance and effective dielectric constant values for the microstrip line. It is given by

$$C = \frac{\sqrt{\epsilon_{re}(L,\ h,\ \epsilon_r)}}{cZ_0(L,\ h,\ \epsilon_r)} W_e \tag{2.79}$$

Here, W_e is the effective width of the microstrip line [see (B.13) in Appendix B]. If we now subtract the parallel plate capacitance from (2.79), we obtain the edge capacitances for the above microstrip line at the edges $y = 0$ and $y = W$. This edge capacitance for the microstrip line is the end capacitance for the patch. Thus,

$$\Delta C = \frac{1}{2}\left\{\frac{\sqrt{\epsilon_{re}(L,\ h,\ \epsilon_r)}}{cZ_0(L,\ h,\ \epsilon_r)} - \frac{\epsilon_0 \epsilon_r L}{h}\right\} W_e \tag{2.80}$$

and

$$B_s = \omega \Delta C = \pi f\left\{\frac{\sqrt{\epsilon_{re}(L,\ h,\ \epsilon_r)}}{cZ_0(L,\ h,\ \epsilon_r)} - \frac{\epsilon_0 \epsilon_r L}{h}\right\} W_e \tag{2.81}$$

The value of W_e as a function of W, h, and ϵ_r for a microstrip line can be obtained as demonstrated in Appendix B.

Wide patch approximation, based on the Wiener-Hopf approach, yields the following expression for the end susceptance [68]:

$$\begin{aligned} B_s &= Y_0 \tan(\beta \Delta \ell) \qquad (2.82a) \\ &= 0.01668 \frac{\Delta \ell}{h} \frac{W_e}{\lambda_0} \epsilon_{re} \end{aligned}$$

where

$$\frac{\Delta \ell}{h} = \frac{0.95}{1 + 0.85 k_0 h} - \frac{0.075(\epsilon_r - 2.45)}{1 + 10 k_0 h} \tag{2.82b}$$

The accuracy of (2.82b) is 2% for $0.1 < k_0 h < 0.6$ and $2.45 < \epsilon_r < 2.65$. Comparison of values obtained from (2.81) with (2.82) shows that the value of the edge susceptance is very similar in the two cases for $0.25\lambda_0 < W < 0.6\lambda_0$. However, (2.81) may be preferred because there is no restriction on the value of the patch width for this formula. More rigorous characterization of the open-edge susceptance has been reported in [73–77]. The closed-form expression reported in [76] for the open-end extension of the radiating edge is given as follows:

$$\frac{\Delta \ell}{h} = \frac{\zeta_1 \zeta_3 \zeta_5}{\zeta_4} \tag{2.83}$$

where ζ_1, ζ_3, ζ_4, ζ_5, and so on are defined in Appendix B. Equation (2.83) is very accurate and is normally used for the open-end extension and the open-end susceptance.

2.8 Mutual Admittance, Y_m

It is known from the analysis of microstrip patch antennas that mutual coupling between the edges plays an important role in the accurate determination of input impedance. This information is also needed in determining the mutual coupling between the patches for antenna array design. The mutual admittance between the radiating edges is included explicitly in the equivalent circuits for the transmission line model and the multiport network model. In the cavity model, the mutual conductance effect is included implicitly in the calculation of the effective loss tangent through the power radiated. Closed-form expressions for the mutual admittance between the apertures are very few. The expressions available in [4, Chapter 9] are given next.

2.8.1 Mutual Conductance, G_m

The mutual conductance G_m between finite length slots has been derived from a knowledge of the mutual conductance between infinite slots. Therefore, mutual conductance is defined as [4, Chapter 9]

$$G_m = G_s F_g \tag{2.84}$$

Here, G_s is the self-conductance of a finite length slot. The factor F_g accounts for mutual coupling between the slots. Its value is assigned to be the same as would exist in infinitely long slots, and is therefore defined as

$$F_g = g_m / g_s \tag{2.85}$$

where g_s and g_m are the per unit length self-conductance and mutual conductance, respectively, of two infinitely long TE excited slots in a perfectly conducting plane. The slots are shown in Figure 2.20. The expression for g_s was derived in Section 2.7.1 and is given by (2.66). The expression for g_m can also be derived in an analogous manner. For this, the mutual power between the coupled slots is determined by taking the Fourier transform of the slot fields,

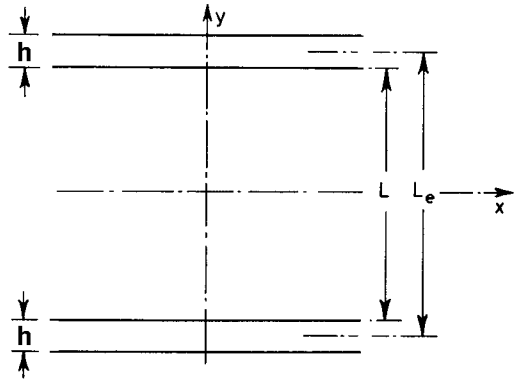

Figure 2.20 Geometry to determine mutual coupling between two infinitely long slots.

similar to (2.63a). By virtue of the separation L_e between the slots, the expression for g_m gets modified to

$$g_m = \frac{k_0}{\pi\eta_0}\int_0^{+k_0} \frac{\sin^2(k_y h/2)}{(k_y h/2)^2}\cos(k_y L_e)\frac{dk_y}{\sqrt{k_0^2 - k_y^2}} \tag{2.86}$$

where L_e is the center distance between the two slots. The integral in (2.86) is approximated to yield

$$g_m \approx \frac{k_0}{2\eta_0}\left\{\left(1 - \frac{s^2}{24}\right)J_0(\ell) + \frac{s^2}{24}J_2(\ell)\right\} \tag{2.87}$$

where $s = k_0 h$ and $\ell = k_0 L_e$. Using (2.66) for g_s and (2.87) for g_m in (2.85), one obtains

$$F_g \approx J_0(\ell) + \frac{s^2}{24 - s^2}J_2(\ell) \tag{2.88}$$

Mutual conductance obtained from (2.84) has been compared with the mutual conductance of the four-slot arrangement, as shown in Figure 2.4(b). The agreement is found to be reasonable justifying the above model for mutual conductance.

2.8.2 Mutual Susceptance, B_m

The modeling for B_m is similar to that for G_m, except for another correction factor, that is,

$$B_m = B_s F_b K_b \tag{2.89}$$

The factor F_b is defined as

$$F_b = \frac{b_m}{b_s} = \frac{\pi}{2} \frac{Y_0(\ell) + \dfrac{s^2}{24 - s^2} Y_2(\ell)}{\ln\left(\dfrac{s}{2}\right) + \gamma - 1.5 + \dfrac{s^2/12}{24 - s^2}}, \quad s = k_0 h \quad \ell = k_0 L_e \tag{2.90}$$

where $\gamma = 0.577216$. The correction factor K_b is given by

$$K_b = 1 - \exp(-0.21 k_0 W) \tag{2.91}$$

where W is the slot width.

The expressions for mutual conductance and mutual susceptance, (2.84) and (2.89), respectively, are applicable to any pair of radiating slots belonging to the same patch or different patches.

The calculation of a mutual coupling network for use in MNM is carried out numerically. In this case, the aperture fields at the edges are first converted into equivalent magnetic currents as

$$\vec{M} = -\hat{n} \times \vec{E}_0 h$$

Now each line source of magnetic current is divided into a number of small sections, of length $d\ell$. The number of sections is equal to the number of ports. The magnetic field produced by each section of line source 1 at any section of line source 1 or 2 can be written by using the fields of a magnetic current dipole in free space. This magnetic field yields the induced current density

$$\vec{J}_j = \hat{n} \times \vec{H}_j \tag{2.92}$$

Finally, the mutual admittance between sections i and j is given by [4, Chapter 9]

$$Y_{ji} = J_j d\ell_j / M_i \tag{2.93}$$

Note that in all the expressions given above for self- and mutual admittances, the effective slot length W_e *should be used in place of physical length* W. The relationship between W_e and W for a microstrip line is given in (B.13) of Appendix B.

2.9 Model for Coaxial Probe in Microstrip Antennas

Coaxial probe feed of microstrip antennas is a convenient and useful excitation mechanism. In the full-wave techniques of antenna analysis, the excitation is treated as an integral part of the antenna and the input impedance is calculated. The probe reactance can be extracted from these data as described later in Figure 2.23. The analytical models, on the other hand, employ an ideal feed. The feed is modeled separately and its reactance calculated and added to the input impedance of the patch antenna. In the cavity model analysis of patch antennas in Section 2.3, however, the entire coaxial feeding structure is modeled as a thin strip of finite width of uniformly distributed electric current flowing vertically from the ground plane to the patch. The probe reactance in the model appears as an inductance associated with the nonresonant modes of the cavity. For a rectangular patch antenna, the probe reactance obtained from (4.19) is

$$X_p = \omega\mu_0 h \sum_m \sum_{n=0}^{\infty} \frac{\psi_{mn}^2(x_0, y_0)}{k_{mn}^2 - k^2} G_{mn} \tag{2.94}$$

where $m = 1$, $n = 0$ mode is excluded, and

$$G_{mn} = \operatorname{sinc}(m\pi D_x/(2L)) \operatorname{sinc}(n\pi D_y/(2W))$$

$$\psi_{mn}(x, y) = \sqrt{\frac{\epsilon_m \epsilon_n}{LW}} \cos(k_m x) \cos(k_n y)$$

Here $\epsilon_p = 1$ for $p = 0$ and $\epsilon_p = 0$ for p not equal to zero.

In this model the probe is modeled as a strip of dimensions $D_x \times D_y$ carrying a uniform current. Equation (2.94) includes the effect of feed position (x_0, y_0) substrate parameters, patch size and shape, and the probe dimensions. This model is shown to predict feed inductance that track the measured result reasonably well at all feed locations not too close to the edge of the patch. For

feed locations on or near the edge, the model is found to predict inductances that are too high due to the image produced by the magnetic wall [78].

A number of models have been advanced to model the probe reactance. In these models, a canonical problem of a probe inside a parallel plate waveguide is solved. By image theory, it is easily seen that the constant cylindrical current between two infinite parallel plates is equivalent to an infinite cylinder with a constant current density. The impedance per unit length of the infinite cylinder can be obtained in a straightforward manner [79]. This leads to the following expression for the probe impedance in the presence of two infinite plates [61]:

$$Z_p = \frac{\omega\mu_0 h}{4} H_0^{(2)}(kp) J_0(kp) \quad \text{for } k = k_0\sqrt{\epsilon_r} \tag{2.95a}$$

Here, p is the probe radius. For small kp values ($kp < 1$), this formula reduces to [80, 81]

$$Z_p = \frac{\omega\mu_0 h}{4} + j\frac{\omega\mu_0 h}{2\pi}\left[\ln\left(\frac{2}{kp}\right) - \gamma\right] \tag{2.95b}$$

where $\gamma = 0.57721$ is the Euler constant. When the substrate thickness increases, the current distribution is no longer constant. An integral equation approach leads to the following expression [82, 83]:

$$Z_p = \frac{60\pi}{\sqrt{\epsilon_r}} \frac{\tan^2(kh/2)}{kh/2} + j\frac{120}{\sqrt{\epsilon_r}} \tan(kh/2) \ln\left(\frac{1.125}{kp}\right) \tag{2.95c}$$

An actual coaxial feed produces a radial electric field in the coaxial aperture. The equivalent current in this excitation model is a ring of magnetic current on the ground plane acting in the presence of the probe [78]. The magnetic current induces current on the probe. In a more rigorous approach an incident TEM wave in the coaxial aperture is assumed [80]. This approach is described next.

Consider the geometry of a coaxial line with a truncated outer conductor flush mounted to the lower conducting plate of a parallel plate waveguide as shown in Figure 2.21(a). The inner conductor passes through the parallel plate region and is attached to the upper conducting plane. The magnetic current model of the aperture is used here. The radial transmission line mode and all higher order modes in the parallel plate region are determined from the excitation. The probe admittance is obtained by enforcing the continuity of complex

Figure 2.21 (a) Configuration of the junction between coaxial probe and parallel plates. (From [80]. © 1991 IEEE. Reprinted with permission.) (b) Equivalent circuit for the probe impedance in part (a).

power flow at the coaxial aperture. Under the assumption of $(kh)^2 << \pi$ and $(kd)^4 << 1$, the probe admittance can be expressed as [80]

$$Y_{\text{probe}} = [R_p + j\omega(L_p + L_0)]^{-1} + j\omega C_0 \tag{2.96}$$

where

$$R_p = \omega\mu_0 h/4 \tag{2.97}$$

$$L_p = \frac{\mu_0 h}{2\pi}\left[\ln\left(\frac{2}{kp}\right) - \gamma\right] \tag{2.98}$$

$$C_0 = \frac{\epsilon_0\epsilon_r}{6hg^2}\left\{3\pi[d^2 - p^2 - 2d^2 g] + 4\pi h^2 g - \frac{12h^3}{\pi^2 d}\left(1.202 - \sum_{n=1}^{\infty} n^{-3}\exp[-2n\pi(d-p)/h]\right)\right\} \tag{2.99}$$

$$L_0 = \frac{-\mu_0 h k^2}{4\pi g}[g(d^2 + p^2) - d^2 + p^2]\left[\ln\left(\frac{kp}{2}\right) + \gamma\right] \tag{2.100}$$

$$g = \ln(d/p)$$

where d is the radius of the relief hole as shown in Figure 2.21(a). The equivalent circuit for the probe, based on the probe admittance (2.96), is shown in Figure 2.21(b). It has been suggested that this equivalent circuit can be used even when the infinite parallel plate is replaced by a finite sized patch and *the probe is not located very close to the edge of the patch*. According to (2.96), the probe impedance is not a function of probe position. Experience, however, indicates that probe reactance varies with feed location. The measured feed reactance is compared with the computed value in Figure 2.22 [78]. For unloaded patch antennas, this variation may not be a very significant design consideration because the resonant reactance often strongly dominates the feed reactance near the resonant frequency. In such cases, the feed reactance from (2.96) can be used. However, in a patch loaded with slots, shorts, or varactor diodes, the resonant frequency is different from the unloaded patch and the resonant reactance [78] may no longer dominate the feed reactance. Equation (2.96), therefore, should not be used for a loaded patch. One can use numerical techniques to calculate the antenna performance or measure the feed reactance in such a situation. A typical plot of input impedance versus frequency is

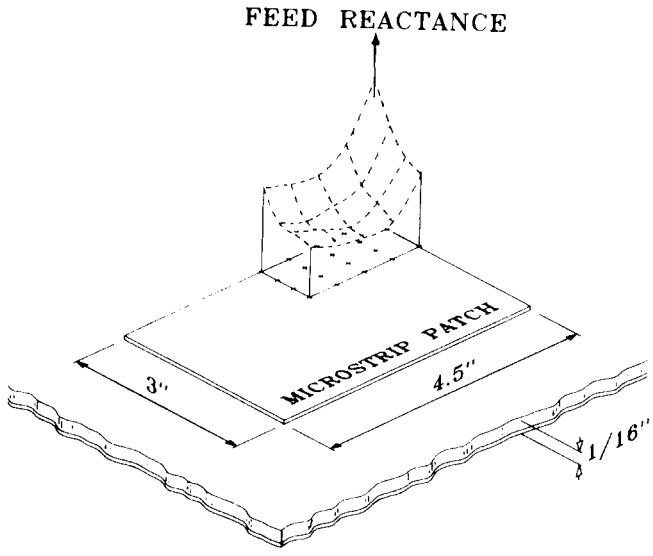

Figure 2.22 Measured feed reactance at 1400 MHz for a rectangular patch. (From [78]. © 1983 *Electromagnetics*. Reprinted with permission.)

shown in Figure 2.23 for a rectangular patch. From the $X_{\min}$ and $X_{\max}$ values, the probe reactance or feed reactance is given by

$$X_p = \frac{1}{2}(X_{\min} + X_{\max}) \tag{2.101}$$

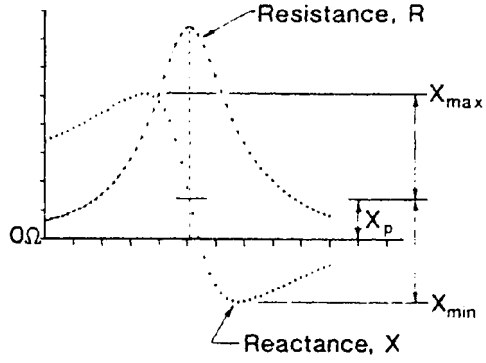

Figure 2.23 Figure illustrating the extraction of feed reactance from a typical impedance curve for a resonant microstrip antenna.

2.10 Comparison of Analytical Models

The various models discussed so far can be grouped into two categories: transmission line models and cavity models. The transmission line model (Section 2.2.1) is easy to implement and the effect of mutual coupling between radiating edges is included explicitly through loads. The effect of surface wave power loss can be included through additional load conductance. The major drawback of this model is that the fields along the width of the patch and the substrate thickness are assumed to be uniform. Therefore, this model is restricted to the rectangular patch geometry, thin substrate, single-layer, linearly polarized antennas, and to probe feed and microstrip edge feed. Array antennas of rectangular patches can be analyzed. However, GTLM (Section 2.2.3) is generalized to include variation of fields in the transverse direction also. Therefore, it can be used to analyze almost all of the useful practical microstrip antennas, circularly polarized antennas, and array antennas. However, its application is limited to thin substrate, nonstacked antennas and to probe feed and microstrip edge feed. The lossy transmission line model (Section 2.2.4) is generalized to analyze arbitrarily shaped patches, stacked geometry, and proximity coupling. The mutual coupling in this model is included implicitly. Therefore, it is not accurate for array antennas.

The cavity models of Sections 2.3 and 2.4 are basically lossy cavity models. The mutual coupling between the radiating edges is included implicitly in the form of radiated power, which accounts for the effect of mutual conductance only. The mutual susceptance is not accounted for. Surface wave power loss can also be included as a general loss term. The cavity model has been generalized to include the variation of fields along the substrate thickness, aperture coupling to microstrip line, and stacked patch configuration. Mutual coupling between rectangular patches has been determined from the magnetic current model as in the case of the transmission line model. However, application of this approach to arrays is limited because in this model, fields from various apertures are assumed to be in phase. The radiation and mutual coupling effects are incorporated explicitly through the lumped loads in the multiport network model (MNM). Variation of the fields along the width of the patch is also included as in the cavity model. Its main limitation is that the variation of fields along the substrate thickness is not included. It has not been applied to a multilayered geometry or aperture coupling. Based on this discussion, a comparison of the various analytical models appears in Table 2.1.

A major drawback of the analytical models is the limited accuracy in resonant frequency and input impedance for the substrates that are not thin. Also, they have a limited capacity to handle problems such as mutual coupling, large arrays, surface wave effects, and different substrate configurations [1].

Table 2.1
Comparison of Various Analytical Models

Application	Model: Transmission Line Model	GTLM	Lossy Transmission Line Model	Cavity Model	Generalized Cavity Model	MNM
Patch shapes analyzed	Rectangular only	Separable geometries	Arbitrary shapes	Regular shapes	Separable geometries	Separable geometries
Substrate thickness	Thin	Thin	Thin	Thick	Thin	Thin
Feed types used	Microstrip edge feed, probe feed	Microstrip edge feed, probe feed	Possibly all types	Microstrip edge feed, probe feed, aperture coupling	Microstrip edge feed, probe feed	Microstrip edge feed, probe feed, proximity coupling
Circularly polarized antenna	No	Yes	No	Yes	Yes	Yes
Stacked antennas	No	No	Yes	Yes	No	No
Mutual coupling between edges	Explicitly included	Explicitly included	Implicitly included	Implicitly included	Implicitly included	Explicitly included
Application to arrays	Yes	Yes	No	No	No	Yes

Full-wave numerical techniques can provide analysis of the microstrip antenna in which all effects, such as space wave radiation, surface wave loss and coupling, mutual coupling between the edges, fringing fields, and so on, do not have to be modeled. These features are all integrated in the analysis technique through an accurate Green's function. These techniques are very accurate and powerful, and are discussed in the next chapter. The FDTD technique is also discussed there, and can be used to include the effect of finite substrate size and ground plane.

Appendix 2A: Theoretical Background of the Generalized Transmission Line Model

The generalized transmission line model (GTLM) [5, 14], in principle, can be applied to any microstrip antenna that has a separable geometry. A large number of practically used patches comes under this category. The theoretical background of this model is presented in this appendix.

2A.1 Introduction

Two different types of possible microstrip patch configurations with separable geometries are shown in Figure 2.24. The patch in Figure 2.24(a) has two radiating edges defined by $u = u_1$ and $u = u_2$ in the curvilinear coordinate (u-v) system. On the other hand, the patch in Figure 2.24(b) has four edges defined by $u = u_1$, $u = u_2$, $v = v_1$, and $v = v_2$. The circular ring is an example of the first kind [see Figure 2.24(a)] and a rectangular patch is an example of the second kind [see Figure 2.24(b)]. The circular patch has only one radiating edge and comes under the first kind when the inner radiating contour ($u = u_1$) has a vanishingly small area (converges to a point).

To develop the model, we start with the field configuration under the patch metalization. The longitudinal component (z component) of the electric field underneath the patch is a solution of the following wave equation (a time dependence $e^{j\omega t}$ is assumed):

$$\nabla^2 E_z + k^2 E_z = 0 \tag{2A.1}$$

where ∇^2 is the Laplacian operator and k is the wave number in the substrate on which the patch is etched. In a practical microstrip antenna, the substrate thickness h is very small compared to the wavelength in the dielectric medium (typically $h\sqrt{\epsilon_r}/\lambda_0 < 0.04$). The electric field E_z, therefore, can be regarded

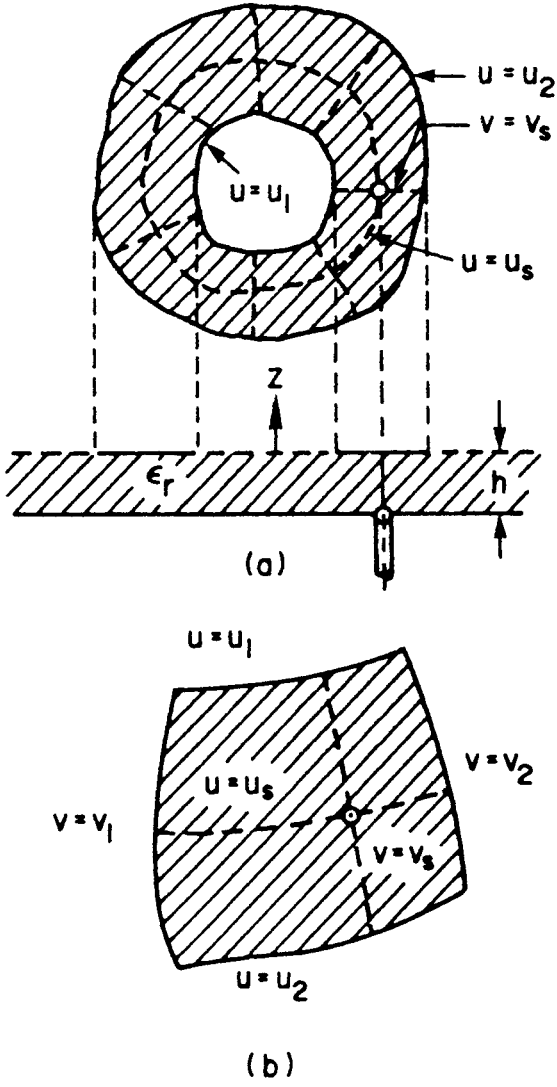

Figure 2.24 Two possible microstrip patch configurations with separable geometry. (From [5]. © 1985 IEE. Reprinted with permission.) (a) Geometry with two edges and (b) geometry with four edges.

as constant along z. Equation (2A.1) can then be written in the curvilinear coordinate system as [77]

$$\frac{1}{h_1 h_2}\left[\frac{\partial}{\partial u}\left(\frac{h_2}{h_1}\frac{\partial E_z}{\partial u}\right) + \frac{\partial}{\partial v}\left(\frac{h_1}{h_2}\frac{\partial E_z}{\partial v}\right)\right] + k^2 E_z = 0 \qquad (2A.2)$$

where h_1 and h_2 are scale factors along the u and v directions, respectively, and are defined as

$$h_1 = \left|\frac{\partial \vec{r}}{\partial u}\right|, \quad h_2 = \left|\frac{\partial \vec{r}}{\partial v}\right|$$

where $\vec{r}$ is the position vector. It is assumed in this model that the patch configurations under consideration are separable, that is, the solution for E_z in (2A.2) can be expressed as

$$E_z(u, v) = f_1(u) f_2(v) \tag{2A.3}$$

Substituting (2A.3) in (2A.2) and dividing the resulting equation by $f_1(u) f_2(v)$, one obtains

$$\frac{1}{h_1 h_2}\left[\frac{1}{f_1}\frac{\partial}{\partial u}\left(\frac{h_2}{h_1}\frac{\partial f_1}{\partial u}\right) + \frac{1}{f_2}\frac{\partial}{\partial v}\left(\frac{h_1}{h_2}\frac{\partial f_2}{\partial v}\right)\right] + k^2 = 0 \tag{2A.4}$$

Let $h_2/h_1 = p(u, v)$ and $h_1 h_2 = q(u, v)$. Then (2A.4) becomes

$$\frac{p}{f_1}\frac{\partial^2 f_1}{\partial u^2} + \frac{1}{f_1}\frac{\partial p}{\partial u}\frac{\partial f_1}{\partial u} + \frac{1}{f_2 p}\frac{\partial^2 f_2}{\partial v^2} - \frac{1}{f_2}\frac{1}{p^2}\frac{\partial p}{\partial v}\frac{\partial f_2}{\partial v} + k^2 q = 0 \tag{2A.5}$$

The above bivariate equation can be separated into two single variable differential equations if either

$$p(u, v) = g(u) f(v) \text{ and } p(u, v) q(u, v) = [m_1(u) + m_2(v)] f^2(v) \tag{2A.6a}$$

or

$$p(u, v) = g(u)/f(v) \text{ and } q(u, v)/p(u, v) = [m_1(u) + m_2(v)]/g^2(u) \tag{2A.6b}$$

Apparently, (2A.6a) and (2A.6b) appear to be two distinct criteria for the separability of (2A.5). However, if one solves for either from (2A.6a) or from (2A.6b), one can see that they assume similar forms. Therefore, without loss of generality, one can consider that (2A.6a) holds. Equation (2A.5) can then be separated as

$$\frac{g^2}{f_1}\frac{\partial^2 f_1}{\partial u^2} + \frac{g}{f_1}\frac{\partial g}{\partial u}\frac{\partial f_1}{\partial u} + k^2 m_1(u) = \alpha^2 \tag{2A.7a}$$

and

$$\frac{1}{f^2}\frac{1}{f_2}\frac{\partial^2 f_2}{\partial v^2} - \frac{1}{f^3}\frac{1}{f_2}\frac{\partial f}{\partial v}\frac{\partial f_2}{\partial v} + k^2 m_2(u) = -\alpha^2 \tag{2A.7b}$$

where α is a constant, independent of u and v. Equations (2A.7a) and (2A.7b) can be rewritten as

$$\frac{\partial^2 f_1}{\partial u^2} + \frac{1}{g}\frac{\partial g}{\partial u}\frac{\partial f_1}{\partial u} + \frac{k^2 m_1 - \alpha^2}{g^2} f_1 = 0 \tag{2A.8}$$

and

$$\frac{\partial^2 f_2}{\partial v^2} - \frac{1}{f}\frac{\partial f}{\partial v}\frac{\partial f_2}{\partial v} + (k^2 m_2 + \alpha^2) f^2 f_2 = 0 \tag{2A.9}$$

Equations (2A.8) and (2A.9) are second-order nonlinear (in general) differential equations. Each of them will have two independent solutions. Let $x_1(u)$ and $x_2(u)$ be the two solutions of (2A.8). The general solution for E_z will be then

$$E_z(u, v) = \begin{Bmatrix} x_1(u) \\ x_2(u) \end{Bmatrix} f_2(v) \tag{2A.10}$$

Having determined E_z as above, the magnetic field components are obtained through the Maxwell's equation $\nabla \times \vec{E} = -j\omega\mu\vec{H}$. One obtains

$$H_u = \frac{1}{-j\omega\mu h_2}\frac{\partial E_z}{\partial v} = \frac{1}{-j\omega\mu h_2} f_1(u) f_2'(v) \tag{2A.11}$$

and

$$H_v = \frac{1}{j\omega\mu h_1}\frac{\partial E_z}{\partial u} = \frac{1}{j\omega\mu h_1} f_1'(u) f_2(v) \tag{2A.12}$$

where a prime indicates the derivative of the function with respect to the argument.

2A.2 Transmission Line Equations

We stated earlier that a patch can be modeled as a transmission line section. The transmission line voltage and the transmission line current are defined next.

In the GTLM, the transmission line is taken along the line joining two radiating apertures. The direction of the transmission line in the case of a patch with two edges, as in Figure 2.24(a), is unique (along the u direction). However, for the patch configuration shown in Figure 2.24(b), two directions may be possible for the transmission line: along the v = constant contour (joining two apertures at $u = u_1$ and $u = u_2$) and along u = constant contour (joining two apertures at $v = v_1$ and $v = v_2$). In principle, one can select any one of the above two directions. The effect of radiation from two connecting apertures will appear in the equivalent circuit through terminating loads. The effect of the other two apertures can be included by considering the transmission line to be lossy. However, to simplify the analysis, one should take the transmission line joining the two apertures that radiate a major portion of the power. From the aperture field distribution one can ascertain which of the apertures is radiating more power. The aperture on which the variation of field is slower will radiate more power.

2A.2.1 Transmission Line in *u* Direction

To characterize a transmission line, the transmission line voltage and the transmission line current should be defined. The definitions of these quantities should be such that they obey the transmission line equation pair (telegraphist equations). For a transmission line in the u direction, the line voltage is defined as

$$V = E_z(u, v) = f_1(u) f_2(v) \tag{2A.13}$$

and the line current is defined as

$$I = -h_2 H_v \quad \text{(along the positive } u \text{ direction)} \tag{2A.14}$$

or, using (2A.12)

$$I = \frac{-h_2}{j\omega\mu h_1} f_1'(u) f_2(v) \tag{2A.15}$$

Differentiating (2A.13) with respect to u, one gets

$$\frac{\partial V}{\partial u} = f_1'(u) f_2(v) = -j\omega\mu \frac{h_1}{h_2} I \quad \text{on using (2A.15)}$$

or, using the definition of p (= h_2/h_1)

$$\frac{\partial V}{\partial u} = -j\omega\mu \frac{I}{p} = \frac{-j\omega\mu}{g(u) f(v)} I \tag{2A.16}$$

Combining (2A.8) and (2A.13), we have

$$\frac{\partial^2 V}{\partial u^2} + \frac{1}{g} \frac{\partial g}{\partial u} \frac{\partial V}{\partial u} + \frac{k^2 m_1 - \alpha^2}{g^2} V = 0$$

or

$$\frac{\partial}{\partial u}\left[g \frac{\partial V}{\partial u} \right] + \frac{k^2 m_1 - \alpha^2}{g} V = 0 \tag{2A.17}$$

Substituting the expression for $\partial V/\partial u$ from (2A.16) into (2A.17) gives

$$\frac{\partial I}{\partial u} - \frac{f(v)(k^2 m_1 - \alpha^2)}{j\omega\mu g(u)} V = 0 \tag{2A.18}$$

Equations (2A.16) and (2A.18) are the transmission line equations. The transmission line parameters obtained from these equations are:

$$\text{Shunt admittance/length} = \frac{-f(v)(k^2 m_1 - \alpha^2)}{j\omega\mu g(u)} \tag{2A.19}$$

$$\text{Series impedance/length} = \frac{j\omega\mu}{g(u) f(v)} \tag{2A.20}$$

The line parameters being functions of u, the equivalent circuit of the patch is a nonuniform transmission line. Expressions for $f(v)$, $g(u)$, and $m_1(u)$ are dictated by the geometry of the separable patch. The constant α, however, depends on the *mode* of operation. The value of α is obtained from the solution of (2A.9) with appropriate boundary conditions. When the radiating contours are closed as in Figure 2.24(a), the function $f_2(v)$ must be a periodic function of v and the α values are discrete in nature. Each value of α is associated with

a mode. Therefore, a transmission line mode is designated by a single index (corresponding to the value of α). When the radiating contours are not closed [as in Figure 2.24(b)], the value of α, in general, will be complex due to leakage of power through the apertures at $v = v_1$ and $v = v_2$. The line voltage and the line current of a transmission line in the v direction are considered next.

2A.2.2 Transmission Line in *v* Direction

For the transmission line in the v direction, the line voltage is defined as

$$V = E_z(u, v) \tag{2A.21a}$$

and the line current is defined as

$$I = \frac{-h_2 H_u}{f(v)} \quad \text{(along the positive } v \text{ direction)} \tag{2A.21b}$$

Combining (2A.9), (2A.11), and (2A.21), we have

$$\frac{\partial V}{\partial v} = j\omega\mu f(v) I \tag{2A.22}$$

and

$$\frac{\partial I}{\partial v} = \frac{-f(v)}{j\omega\mu}(k^2 m_2(v) + \alpha^2) V \tag{2A.23}$$

Because the line voltage and the line current again satisfy the transmission line equations, (2A.22) and (2A.23), the line parameters of the nonuniform transmission line can be obtained from these equations.

In the preceding sections, the line voltages and the line currents for two possible transmission lines were defined. The equivalent circuit of a nonuniform transmission line section is obtained in the following section.

2A.3 Equivalent Circuit of a Nonuniform Transmission Line Section

In this section, the equivalent Π network of a transmission line section is obtained. We concentrate on the u-directed transmission line here. The equiva-

lent Π network of a transmission line in the v direction can be obtained in a similar manner.

A transmission line section confined in the region $u_1 < u < u_2$ (nonuniform in general) and its equivalent Π network are shown in Figure 2.25. Elements of the equivalent Π network are obtained from the Y matrix of the transmission line section. The Y matrix is defined as

$$\begin{bmatrix} I_1 \\ I_2 \end{bmatrix} = \begin{bmatrix} Y_{11} & Y_{12} \\ Y_{21} & Y_{22} \end{bmatrix} \begin{bmatrix} V_1 \\ V_2 \end{bmatrix} \tag{2A.24}$$

The port currents I_1, I_2 and the port voltages V_1, V_2 are shown in Figure 2.25. The elements of the Y matrix are obtained from the following equations:

$$\begin{aligned} Y_{11} &= I_1/V_1 \quad (\text{when } V_2 = 0) \\ Y_{12} &= I_1/V_2 \quad (\text{when } V_1 = 0) \\ Y_{21} &= I_2/V_1 \quad (\text{when } V_2 = 0) \text{ and} \\ Y_{22} &= I_2/V_2 \quad (\text{when } V_1 = 0) \end{aligned}$$

Here, V is the line voltage and is given by

$$V = E_z = \{A_{x_1}(u) + B_{x_2}(u)\} f_2(v) \tag{2A.25}$$

and the line current along the u direction is given by (2A.15), that is,

$$I = \frac{-1}{j\omega\mu} \frac{h_2}{h_1} \{A_{x_1'}(u) + B_{x_2'}(u)\} f_2(v) \tag{2A.26}$$

where A and B are constants, and $x_1(u)$ and $x_2(u)$ are the independent solutions of (2A.8). Now, $V_2 = V(u = u_2) = 0$ is satisfied if

$$B/A = -x_1(u_2)/x_2(u_2)$$

The expression for Y_{11} thus becomes

$$Y_{11} = \frac{I_1}{V_1} = \frac{I(u = u_1)}{V(u = u_1)} = \frac{-h_2}{j\omega\mu h_1} \left\{ \frac{x_2(u_2)x_1'(u_1) - x_1(u_2)x_2'(u_1)}{x_2(u_2)x_1(u_1) - x_1(u_2)x_2(u_1)} \right\} \tag{2A.27}$$

Similarly,

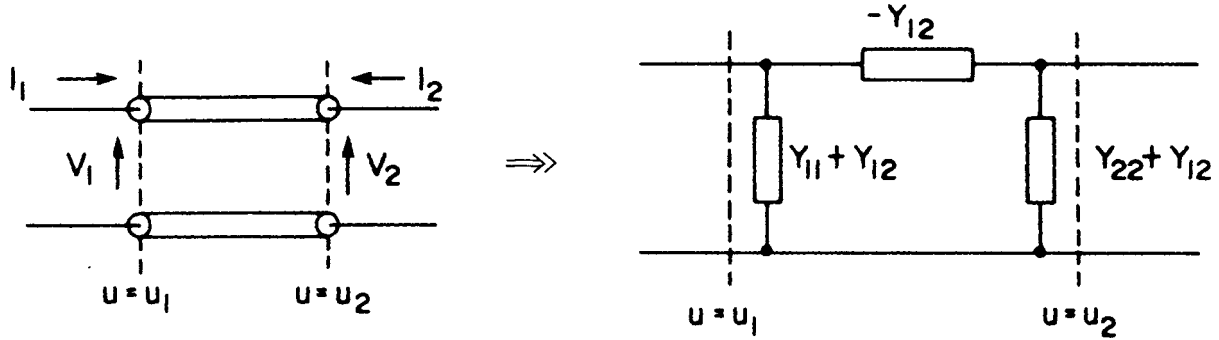

Figure 2.25 A nonuniform transmission line section and the equivalent Π network. (From [5]. © 1985 IEE. Reprinted with permission.)

$$Y_{22} = \frac{-I(u = u_2)}{V(u = u_2)} \quad (\text{when } V(u = u_1) = 0) \tag{2A.28}$$

$$= \frac{h_2}{j\omega\mu h_1}\left\{\frac{x_2(u_1)x_1'(u_2) - x_1(u_1)x_2'(u_2)}{x_2(u_1)x_1(u_2) - x_1(u_1)x_2(u_2)}\right\}$$

Note that the ratio h_2/h_1 in (2A.27) should be evaluated at $u = u_1$, whereas this ratio should be evaluated at $u = u_2$ for (2A.28). The expression for Y_{12} is given by

$$Y_{12} = \frac{1}{j\omega\mu}\frac{h_2}{h_1}\left\{\frac{x_2(u_1)x_1'(u_1) - x_1(u_1)x_2'(u_1)}{x_2(u_1)x_1(u_2) - x_1(u_1)x_2(u_2)}\right\} \tag{2A.29}$$

In a similar manner one can derive the expression for Y_{21} and can verify that

$$Y_{21} = Y_{12} \tag{2A.30}$$

The relationship just given confirms the transmission line section to be a reciprocal device, and therefore a Π-network model of the device is possible. This relationship also justifies the definition of the line voltage and line current used in (2A.13) and (2A.14), respectively. When a patch is excited by a source placed at $u = u_s$, the patch can be modeled as a combination of two transmission line sections defined by $u_1 < u < u_s$ and $u_s < u < u_2$. Each of these transmission line sections can be represented by a Π network as shown in Figure 2.25. The elements of the Y matrix for the section defined by $u_1 < u < u_s$ can be obtained by replacing u_2 by u_s in (2A.27), (2A.28), and (2A.29). Similarly, for the section defined by $u_s < u < u_2$, the matrix elements are obtained by replacing u_1 with u_s in these equations. The equivalent circuit of the patch with source is shown in Figure 2.26. This network accounts for the energy stored under the patch metalization and the dielectric loss for an imperfect dielectric substrate and the loss of power due to the leakage through the side walls at $v = v_1$ and $v = v_2$. To incorporate the effects of radiated power through the main radiating apertures, the circuit should be terminated with appropriate radiation admittances. This is considered next.

2A.4 Radiation Admittance

A radiating aperture can be characterized by an equivalent admittance, the susceptance being due to the stored energy in the fringing fields and the

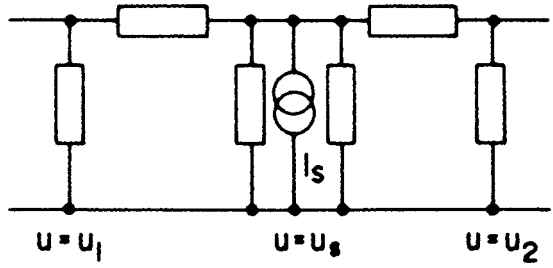

Figure 2.26 Equivalent circuit representation of the patch in terms of equivalent Π networks. (From [16]. © 1991 Elsevier Science Publishing. Reprinted with permission.)

conductance being due to the power loss from radiation. To determine the wall admittance, the magnetic current model can be used. In this model, an aperture is replaced by its equivalent magnetic current. The electromagnetic fields radiated by the equivalent magnetic current are the same as that of the aperture. Because we have two apertures, in general, there should be two equivalent magnetic current sources. The active wall admittance at $u = u_1$ is defined as

$$y_1^a = \frac{-I_t(u_1)}{V(u_1)} \tag{2A.31}$$

where $I_t(u_1)$ is the total induced line current on the aperture at $u = u_1$ due to the magnetic current sources at $u = u_1$ and $u = u_2$. According to the definition of line current in (2A.14), we have

$$I_t(u_1) = -h_2 H_{vt}(u_1)$$

where $H_{vt}(u_1)$ is the total induced magnetic field along v on the aperture at $u = u_1$. This field is the sum of the self magnetic field, $H_{vs}(u_1)$, which is generated by the source at $u = u_1$ and the coupled field, $H_{vm}(u_1, u_2)$, which is generated by the aperture source at $u = u_2$ on the aperture at $u = u_1$. Therefore,

$$H_{vt}(u_1) = H_{vs}(u_1) + H_{vm}(u_1, u_2) \tag{2A.32}$$

The active wall admittance thus becomes

$$y_1^a = \frac{h_2 H_{vs}(u_1)}{E_z(u_1)} + \frac{h_2 H_{vm}(u_1, u_2)}{E_z(u_1)} \tag{2A.33}$$

Let us define the self-admittance of the radiating wall at $u = u_1$ as

$$y_1^s = \frac{h_2 H_{vs}(u_1)}{E_z(u_1)} \tag{2A.34}$$

and the mutual admittance between the two walls as

$$y_{21}^m = \frac{-h_2 H_{vm}(u_1, u_2)}{E_z(u_2)} \tag{2A.35}$$

The negative sign in (2A.35) is taken since the equivalent magnetic currents at $u = u_1$ and $u = u_2$ are oppositely directed. One can obtain self-admittance as a special case (when u_2 approaches u_1) from this definition of mutual admittance. Using (2A.34) and (2A.35) in (2A.33), we get

$$y_1^a = y_1^s - y_{21}^m \frac{E_z(u_2)}{E_z(u_1)} = y_1^s - y_{21}^m \frac{V_2}{V_1} \tag{2A.36}$$

where V_1 and V_2 are the line voltages at ports 1 and 2, respectively. Rearranging (2A.36), we obtain

$$y_1^a = (y_1^s - y_{21}^m) + \frac{V_1 - V_2}{V_1} y_{21}^m \tag{2A.37}$$

Similarly, for the aperture at $u = u_2$ we have

$$y_2^a = (y_2^s - y_{12}^m) + \frac{V_2 - V_1}{V_2} y_{12}^m \tag{2A.38}$$

Reciprocity demands that $y_{12}^m = y_{21}^m$. Therefore, (2A.37) and (2A.38) lead to an equivalent circuit, like that shown in Figure 2.27. This circuit can be used to determine the input impedance seen by the source current I_s. It can also be used to determine the aperture voltages from which the radiation characteristics of a patch can be obtained. Note that the equivalent circuit in Figure 2.27 represents a single mode [for a given value of α in (2A.8)]. Each mode will have a circuit similar to that shown in Figure 2.27. The source current I_s is related to the feed current and the mode of operation. The input impedance seen by the feed is proportional to the impedance seen by I_s for a given mode of operation.

To determine the input impedance seen by I_s, the circuit of Figure 2.27 can be simplified using the star-delta and delta-star transformations [6]. The

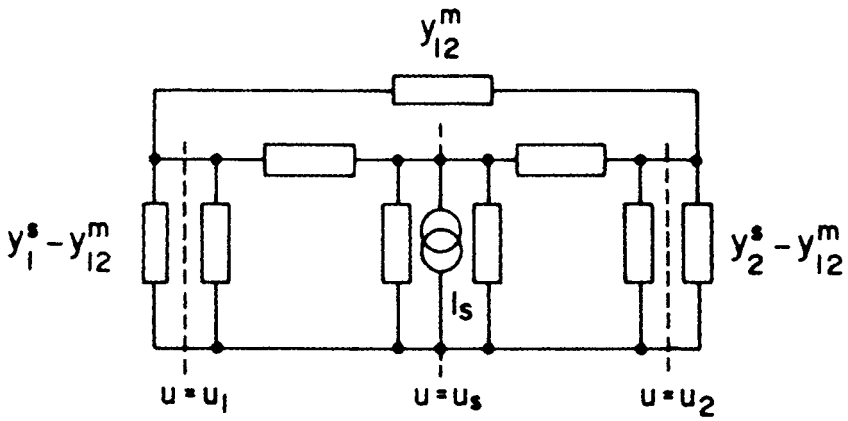

Figure 2.27 GTLM equivalent circuit of the patch antenna for a given transmission line mode. (From [5]. © 1985 IEE. Reprinted with permission.)

impedance seen by the feed current will be obtained if the relation between I_s and the feed current is known. This relationship is derived in the following section. Expressions for the input impedance will also be derived.

2A.5 Input Impedance

Suppose $\hat{z}I_0(v)$ is the feed current distribution (assumed to be a surface current lying on the fictitious surface defined by $u = u_s$). The magnetic field is discontinuous at $u = u_s$ due to the presence of feed current. For a given mode, let the magnetic fields at $u = u_s+$ and at $u = u_s-$ be

$$H_v^{(\alpha)}(u_s+) = A_\alpha^+ f_2^{(\alpha)}(v) \tag{2A.39}$$

$$H_v^{(\alpha)}(u_s-) = A_\alpha^- f_2^{(\alpha)}(v) \tag{2A.40}$$

where $f_2^{(\alpha)}(v)$ is a solution of (2A.9) for a given α. The discontinuity of the magnetic fields yields

$$\sum_\alpha [H_v^{(\alpha)}(u_s+) - H_v^{(\alpha)}(u_s-)] = I_0(v) \tag{2A.41}$$

Now, $-h_2 H_v^{(\alpha)}(u_s+)$ is the line current supplied by the source to the region $u > u_s$, and $h_2 H_v^{(\alpha)}(u_s-)$ is the line current supplied by the source to the region $u < u_s$. Therefore,

$$I_s = -h_2 H_v^{(\alpha)}(u_s+) + h_2 H_v^{(\alpha)}(u_s-) \tag{2A.42}$$
$$= -h_2[A_\alpha^+ - A_\alpha^-]\, f_2^{(\alpha)}(v) = -h_2 B_\alpha f_2^{(\alpha)}(v) \quad \text{(say)}$$

The total current supplied for all the α values should be equal to the feed current $I_0(v)$. Therefore,

$$-\sum_\alpha B_\alpha f_2^{(\alpha)}(v) = I_0(v) \tag{2A.43}$$

It can be proved that the set of functions $f_2^{(\alpha)}(v)$ for various α form an orthogonal set and

$$\int_{v_1}^{v_2} f(v)\, f_2^{(\alpha)}(v)\, f_2^{(\alpha')}(v)dv = 0 \text{ when } \alpha \neq \alpha' \tag{2A.44}$$

Using this orthogonality property, one has from (2A.43)

$$-B_\alpha \int_{v_1}^{v_2} f(v)[f_2^{(\alpha)}(v)]^2 dv = \int_{v_1}^{v_2} f(v)\, f_2^{(\alpha)}(v) I_0(v)dv$$

or

$$B_\alpha = \frac{-\int_{v_1}^{v_2} f(v)\, f_2^{(\alpha)}(v) I_0(v)dv}{\int_{v_1}^{v_2} f(v)[f_2^{(\alpha)}(v)]^2 dv} \tag{2A.45}$$

Substituting for B_α in (2A.42), we get the relationship between the source current I_s and the feed current $I_0(v)$. In particular, when the patch is excited by a probe, the function $I_0(v)$ can be approximated as

$$I_0(v) = I_0 \delta(v - v_s)/h_2(v)$$

where (u_s, v_s) is the feed location. For this case, the expression for B_α reduces to

$$B_\alpha = \frac{-I_0 \dfrac{f(v_s)}{h_2} f_2^{(\alpha)}(v_s)}{\displaystyle\int_{v_1}^{v_2} f(v)[f_2^{(\alpha)}(v)]^2 dv}$$

and (2A.42) gives

$$I_s = \frac{f_2^{(\alpha)}(v) I_0 f(v_s) f_2^{(\alpha)}(v_s)}{\displaystyle\int_{v_1}^{v_2} f(v)[f_2^{(\alpha)}(v)]^2 dv} \tag{2A.46}$$

The input impedance seen by the feed is then given by

$$Z_{in} = \frac{-hE_z(u_s, v)}{I_0} = \frac{E_z}{I_s}\left(\frac{-hI_s}{I_0}\right) = \frac{-hI_s}{I_0} Z_s \tag{2A.47}$$

where Z_s is the impedance seen by I_s (Figure 2.27). The expression for I_s/I_0 can be substituted from (2A.46) to (2A.47) to obtain the impedance seen by the feed current I_0.

Equation (2A.47) yields the input impedance when only one transmission line mode is present. To obtain the total input impedance, individual impedances for all possible modes should be added. However, if the resonant frequencies are not very close to each other as compared to the bandwidth of the operating mode, the contribution of the off-resonant modes will be negligible near the resonance of the operating mode. On the other hand, if some other modes are very close to the operating mode, those mode impedances are to be added. A typical example of this kind is described in Section 2.4.

To determine the impedance seen by I_s in the equivalent circuit of Figure 2.27, the self- and mutual admittances should be known. General expressions for these admittances are provided in the following section.

2A.6 Self- and Mutual Wall Admittances

The magnetic current model can be used to determine the wall admittances of a patch antenna. In this model, the patch is replaced by the equivalent

magnetic current source at its periphery. The wall admittances of the patch are equivalent to the radiation admittances of the corresponding magnetic currents.

The mutual admittance between two edges at $u = u_1$ and $u = u_2$ is defined by (2A.35), that is,

$$y_{12}^m = \frac{-h_2 H_{vm}(u_1, u_2)}{E_z(u_2)} = \frac{h_2 H_{vm}(u_2, u_1)}{E_z(u_1)} \tag{2A.48}$$

where $E_z(u_1) f_2(v)$ and $E_z(u_2) f_2(v)$ are the aperture electric fields at $u = u_1$ and $u = u_2$, respectively. $H_{vm}(u_1, u_2) f_2(v)$ is the magnetic field at $u = u_1$ produced by the source at $u = u_2$. The magnetic field $H_{vm}(u_1, u_2)$ can be determined using the Green's function technique and is given by

$$\overrightarrow{H}_m(u_2, u_1) = \iint_{S_1} \overrightarrow{M}_1 \cdot \overline{\overline{G}}(r_2/r_1) dS_1 \tag{2A.49}$$

where $\overrightarrow{M}_1$ is the equivalent magnetic current on the aperture at $u = u_1$ and is equal to $E_z(u_1)(\hat{z} \times \hat{u}_1)$, $\overline{\overline{G}}$ is the dyadic Green's function that relates the magnetic current to the magnetic field, and s_1 is the surface area of the aperture at $u = u_1$. One can use the free-space Green's function in (2A.49) to determine the mutual admittance. However, to include the effect of substrate, Green's function of a stratified media should be used. For a thin substrate with low dielectric constant ($h\sqrt{\epsilon_r}/\lambda_0 < 0.02$), the effect of substrate is negligibly small and the free-space Green's function yields a good approximation to the mutual admittance.

Although mutual admittance can be calculated using (2A.48), an accurate result is provided by the stationary expression. A stationary expression for the mutual admittance is

$$y_{12}^m = \frac{\langle u_1, u_2 \rangle}{hPE_z(u_1)E_z(u_2)} \quad \text{with } P = \int_{v_1}^{v_2} [f_2(v)]^2 dv \tag{2A.50}$$

In (2A.50), h is the substrate thickness and $\langle u_1, u_2 \rangle$ is the mutual reaction between the sources at $u = u_1$ and $u = u_2$. Because $\langle u_1, u_2 \rangle = \langle u_2, u_1 \rangle$, it follows that $y_{12}^m = y_{21}^m$. If the apertures at $v = v_1$ and $v = v_2$ are considered, the stationary expression for the mutual admittance becomes

$$y_{12}^{m} = \frac{\langle v_1, v_2 \rangle}{hQE_z(v_1)E_z(v_2)} \quad \text{with } Q = \int_{u_1}^{u_2} \frac{f_1^2(u)}{g(u)}\,du \tag{2A.51}$$

where $E_z(v_1)\,f_1(u)$ and $E_z(v_2)\,f_1(u)$ are the aperture electric fields at $v = v_1$ and $v = v_2$, respectively. Equation (2A.50) should be used when the transmission line is along the u direction, and (2A.51) should be used when the transmission line is along the v direction. For the self-admittance, one should use a self-reaction in place of mutual reactions in (2A.50) and (2A.51).

Appendix 2B: Eigenfunctions, Equivalent Dimensions, and Effective Permittivities for Some Patch Shapes With Separable Geometries

The eigenfunctions required for the cavity model analysis of various geometries are given next. *We assume that the dimensions of the patch are not the physical dimensions but the equivalent dimensions, which include the effect of energy stored in the fringing fields*. The equivalent dimensions are also determined.

Rectangle

The eigenfunctions for the rectangle shown in Figure 2.28(a) are given as

$$\psi_{mn}(x, y) = \cos(k_m x)\cos(k_n y) \quad \text{for } m, n = 0, 1, 2, \ldots \tag{2B.1}$$

where

$$k_m = m\pi/L \quad \text{and} \quad k_n = n\pi/W$$

Equilateral Triangle

The eigenfunctions for the triangle shown in Figure 2.28(b) are given as

$$\begin{aligned}\psi_{m,n,\ell}(x, y) = {} & \cos\left(\frac{2\pi x'}{\sqrt{3}a}\ell\right)\sin\left(\frac{2\pi(m-n)y}{3a}\right) \\ & + \cos\left(\frac{2\pi x'}{\sqrt{3}a}m\right)\sin\left(\frac{2\pi(n-\ell)y}{3a}\right) \\ & + \cos\left(\frac{2\pi x'}{\sqrt{3}a}n\right)\sin\left(\frac{2\pi(\ell-m)y}{3a}\right)\end{aligned} \tag{2B.2}$$

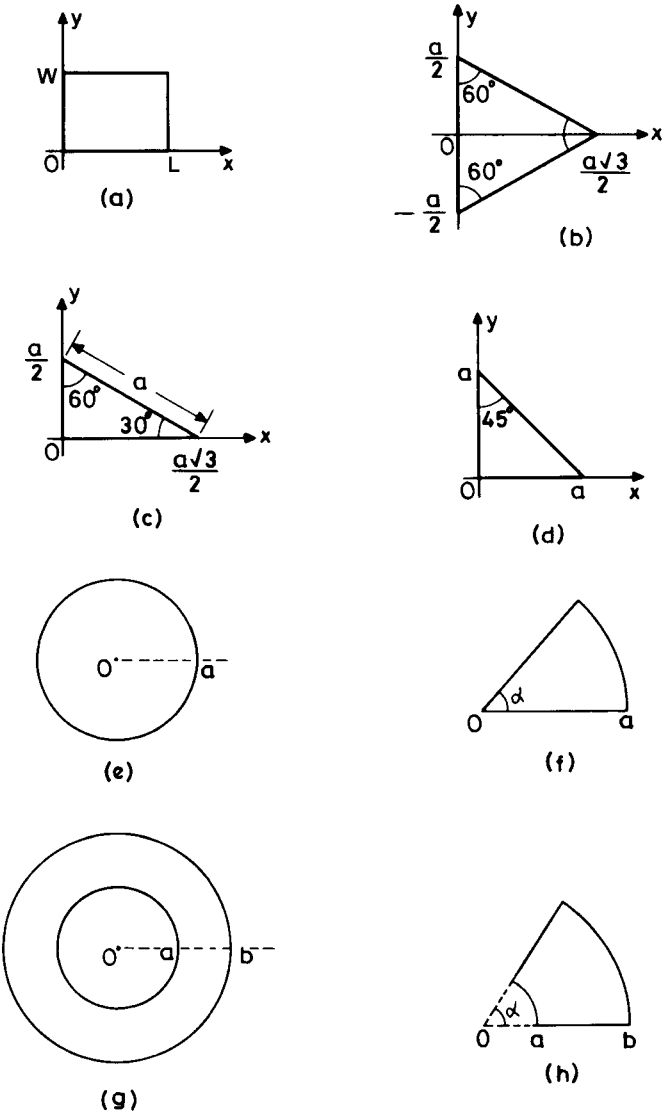

Figure 2.28 Various separable geometries for which eigenfunctions are listed: (a) rectangle, (b) equilateral triangle, (c) 30° and 60° triangles, (d) right-angle isosceles triangle, (e) disk, (f) circular sector, (g) circular ring, and (h) annular sector or circular ring segment.

where

$$x' = x + a/\sqrt{3}, \quad \ell = -(m + n)$$

Thirty- and Sixty-Degree Triangles

The triangle shown in Figure 2.28(c) can be obtained from that of Figure 2.28(b) by placing a magnetic wall at the plane of symmetry. The eigenfunctions for the triangle of Figure 2.28(c) are then obtained as

$$\begin{aligned}\psi_{m,n,\ell}(x, y) = {} & \cos\left(\frac{2\pi x'}{\sqrt{3}a}\ell\right)\cos\left(\frac{2\pi(m-n)y}{3a}\right) \\ & + \cos\left(\frac{2\pi x'}{\sqrt{3}a}m\right)\cos\left(\frac{2\pi(n-\ell)y}{3a}\right) \\ & + \cos\left(\frac{2\pi x'}{\sqrt{3}a}n\right)\cos\left(\frac{2\pi(\ell-m)y}{3a}\right)\end{aligned} \tag{2B.3}$$

where

$$x' = x + a/\sqrt{3}, \quad \ell = -(m + n)$$

Right-Angle Isosceles Triangle

The eigenfunctions for the triangle shown in Figure 2.28(d) are given as

$$\psi_{mn}(x, y) = \cos\frac{m\pi x}{a} - \cos\frac{m\pi y}{a} \tag{2B.4}$$

or

$$\psi_{mn}(x, y) = \cos\frac{m\pi x}{a} \cdot \cos\frac{m\pi y}{a}$$

Disk

The eigenfunctions for the disk shown in Figure 2.28(e) are given as

$$\psi_{mn} = J_n(k_{mn}\rho)\cos n\phi \quad n = 0, 1, 2, \ldots \quad m = 1, 2, 3, \ldots \tag{2B.5}$$

where k_{mn} are the roots of

$$J_n'(k_{mn}a) = 0$$

Circular Sector

The eigenfunctions for circular sectors are available only when the sector angle α is a submultiple of π. For the circular sector shown in Figure 2.28(f), the eigenfunctions are given as

$$\psi_{mv} = J_v(k_{mv}\rho)\cos v\phi \tag{2B.6}$$

where $v = n\pi/\alpha$, and k_{mv} satisfy

$$J_v'(k_{mv}a) = 0$$

Circular Ring

The eigenfunctions for the circular ring shown in Figure 2.28(g) are given as

$$\psi_{mn}(\rho, \phi) = [J_n(k_{mn}\rho)Y_n'(k_{mn}a) - J_n'(k_{mn}a)Y_n(k_{mn}\rho)]\cos n\phi \tag{2B.7}$$
$$n = 0, 1, 2, \ldots \quad m = 1, 2, 3, \ldots$$

where k_{mn} are solutions of

$$J_n'(k_{mn}a)Y_n'(k_{mn}b) - J_n'(k_{mn}b)Y_n'(k_{mn}a) = 0$$

Annular Sector or Circular Ring Segment

As in the case of circular sectors, the eigenfunctions for annular sectors are available only when the sector angle α is a submultiple of π. For the annular sector shown in Figure 2.28(h), the eigenfunctions are given as

$$\psi_{mv}(\rho, \phi) = [J_v(k_{mv}\rho)Y_v'(k_{mv}a) - J_v'(k_{mv}a)Y_v(k_{mv}\rho)]\cos v\phi \tag{2B.8}$$

where $v = n\pi/\alpha$, and k_{mv} are solutions of

$$J_v'(k_{mv}a)Y_v'(k_{mv}b) - J_v'(k_{mv}b)Y_v'(k_{mv}a) = 0$$

Disk With Narrow Slot

The geometry of this antenna is very similar to that of a disk [Figure 2.28(e)], but a narrow slot is cut. However, it is analyzed like a circular sector with $\alpha \approx 2\pi$ and $\nu = n/2$. Therefore, the eigenfunctions for a disk with a narrow slot can be written as

$$\psi_{mn} = J_{n/2}(k_{mn}\rho)\cos(n\phi/2) \tag{2B.9}$$

where k_{mn} satisfy

$$J'_{n/2}(k_{mn}a) = 0 \tag{2B.10}$$

Effective Dielectric Constant and Equivalent Dimensions

The cavity model of the antenna assumes a magnetic wall along the boundary. This involves an outward extension of the physical boundary as shown in Figure 2.10. It implies that the physical dimensions of the patch are replaced by the equivalent dimensions so that the cavity model can predict the resonant frequency accurately. For some of the geometries, the same effect is realized by replacing the permittivity of the substrate by the effective permittivity, whereas in some cases both the effective permittivity and equivalent dimensions are used. In this connection, several methods have been reported in the literature to calculate accurately the resonant frequencies of rectangular patch, circular disk, equilateral triangular patch, and elliptical disk antennas [84–91]. A generalized approach has also been reported for these microstrip antenna geometries [92]. The effective permittivity and equivalent dimensions used in this approach are given next.

Effective Permittivity

The effective relative permittivity of a patch antenna according to [92] is defined as

$$\epsilon_{re} = \frac{\epsilon_r + 1}{2} + \frac{\epsilon_r - 1}{2} F \quad \text{for } 0 < F < 1 \tag{2B.11}$$

The function F is empirically derived from the area occupied by the fringing fields and the area of the patch. It is given by

$$F = 1 - \frac{c_r \epsilon_r}{\epsilon_r - 1} \frac{\text{fringing field area}}{\text{area of the patch}} \tag{2B.12}$$

where $c_r(0)$ is a coefficient to be determined. To determine the area occupied by the fringing fields, they are assumed to extend uniformly over a distance equal to the substrate thickness h. Thus, for an elliptical disk with semi-major axis a and semi-minor axis b, the area occupied by the fringing fields is obtained as

$$\pi(a + h)(b + h) - \pi ab = \pi h(a + b + h) \tag{2B.13}$$

Therefore,

$$F = 1 - \frac{c_r \epsilon_r}{\epsilon_r - 1}\left(\frac{h}{a} + \frac{h}{b} + \frac{h^2}{ab}\right) \tag{2B.14}$$

Use of (2B.14) in (2B.11) gives

$$\epsilon_{re} = \epsilon_r - \frac{c_r \epsilon_r}{2}\left(\frac{h}{a} + \frac{h}{b} + \frac{h^2}{ab}\right) \quad \text{for an elliptical disk} \tag{2B.15}$$

$$\epsilon_{re} = \epsilon_r - \frac{c_r \epsilon_r}{2}\left(\frac{2h}{a} + \frac{h^2}{a^2}\right) \quad \text{for a circular disk or radius } a \tag{2B.16}$$

$$\epsilon_{re} = \epsilon_r - 2c_r \epsilon_r\left(\sqrt{3}\frac{h}{a} + 3\frac{h^2}{a^2}\right)$$

for an equilateral triangular patch of side length a (2B.17)

For a rectangular patch antenna one can use the well-known expression for the effective relative permittivity, (B.4) or (B.12) of Appendix B at the end of the book.

Equivalent Dimensions

The equivalent dimensions of a patch antenna are always larger than the physical dimensions. In the model discussed above for the effective permittivity, the dimensions of the patch antenna are also modified to equivalent dimensions. For a rectangular patch, the equivalent length is obtained by adding the end effect extension $\Delta\ell_\alpha$ on either ends of the patch. An accurate expression for $\Delta\ell_\alpha$ is given in Appendix B in (B.71). The physical width W is replaced by the effective width of the corresponding microstrip line (see Appendix B at the end of the book). For a circular disk of radius a, the equivalent radius is given by

$$a_{eq} = a\left[1 + \frac{2h}{\pi\epsilon_{re}a}\left\{\ln\frac{a}{2h} + (1.41\epsilon_{re} + 1.77) + \frac{h}{a}(0.268\epsilon_{re} + 1.65)\right\}\right]^{1/2} \tag{2B.18}$$

For an equilateral triangular patch, the expression for the equivalent side length is obtained by first converting the triangular patch into a circular disk of equal area. The equivalent radius of this disk is then used to define the effective side length of the triangle. One obtains [92]

$$a_{\text{eff}} = a\left[1 + \frac{2h}{\pi\epsilon_{re}a_{eq}}\left\{\ln\frac{a_{eq}}{2h} + (1.41\epsilon_{re} + 1.77) + \frac{h}{a_{eq}}(0.268\epsilon_{re} + 1.65)\right\}\right]^{1/2} \tag{2B.19}$$

where

$$a_{eq} = \sqrt{A/\pi}, \quad \text{where } A \text{ is the area of the triangular patch}$$

The elliptical disk can be modeled as a circular disk of equal area. For this, the area of an elliptical disk is defined as the geometric mean of the areas of two circular disks with radii a and b, that is, $\pi ab = \sqrt{\pi a^2 \cdot \pi b^2}$. Here, a is the semi-major axis and b is the semi-minor axis of the elliptical disk. The equivalent semi-major axis and semi-minor axis of this disk are obtained from the circular disk of the corresponding radius. The expression for the equivalent semi-major axis a_{eq} for the elliptic disk is therefore given by (2B.18), and the equivalent semi-minor axis b_{eq} is obtained by replacing a and a_{eq} by b and b_{eq}, respectively, in (2B.18).

The value of the constant c_r in (2B.12) is obtained by curve fitting the calculated resonant frequency from the formulas given above with the measured value and/or computed numerical value. An assigned value of 0.7 for c_r for all the patch shapes investigated gives a good match for thin substrates with $h\sqrt{\epsilon_r}/\lambda_0 \leq 0.02$ [92].

References

[1] Pozar, D. M., "Microstrip Antennas," *Proc. IEEE*, Vol. 80, 1992, pp. 79–91.

[2] Carver, K. R., and E. L. Coffey, "Theoretical Investigation of the Microstrip Antenna," Tech. Report PT-00929, Physical Science Laboratory, New Mexico State University, Las Cruces, NM, 1979.

[3] Kishk, A. A., and L. Shafai, "The Effect of Various Parameters of Circular Microstrip Antennas on Their Radiation Efficiency and the Mode Excitation," *IEEE Trans. on Antennas and Propagation*, Vol. AP-34, 1986, pp. 969–976.

[4] James, J. R., and P. S. Hall (Eds.), *Handbook of Microstrip Antennas*, Peter Peregrinus, London, UK, 1989.

[5] Bhattacharyya, A. K., and R. Garg, "Generalised Transmission Line Model for Microstrip Patches," *IEE Proc.*, Vol. 132, Pt. H, 1985, pp. 93–98.

[6] Bhattacharyya, A. K., and R. Garg, "Input Impedance of an Annular Ring Microstrip Antenna Using Circuit Theory Approach," *IEEE Trans. on Antennas and Propagation*, Vol. AP-33, 1985, pp. 217–219.

[7] Bhattacharyya, A. K., and R. Garg, "Analysis of Annular Sector and Circular Sector Microstrip Patch Antennas," *Electromagnetics*, Vol. 6, No. 3, 1986, pp. 229–242.

[8] Munson, R., "Conformal Microstrip Antennas and Microstrip Phased Arrays," *IEEE Trans. on Antennas and Propagation*, Vol. AP-22, 1974, pp. 74–78.

[9] Derneryd, A., "Linearly Polarized Microstrip Antennas," *IEEE Trans. on Antennas and Propagation*, Vol. AP-24, 1976, pp. 846–851.

[10] Derneryd, A., "A Theoretical Investigation of the Rectangular Microstrip Antenna Element," *IEEE Trans. on Antennas and Propagation*, Vol. AP-26, 1978, pp. 532–535.

[11] Lier, E., "Improved Formulas for Input Impedance of Coax-Fed Microstrip Patch Antennas," *IEE Proc.*, Vol. 129, Pt. H, 1982, pp. 161–164.

[12] Pues, H., and A. Van de Capelle, "Accurate Transmission Line Model for the Rectangular Microstrip Antenna," *IEE Proc.*, Vol. 131, Pt. H, 1984, pp. 334–340.

[13] Van Lil, E., and A. Van de Capelle, "Transmission Line Model for Mutual Coupling Between Microstrip Antennas," *IEEE Trans. on Antennas and Propagation*, Vol. AP-32, 1984, pp. 816–821.

[14] Dearnley, R. W., and A. R. F. Barel, "A Broad-Band Transmission Line Model for a Rectangular Microstrip Antenna," *IEEE Trans. on Antennas and Propagation*, Vol. AP-37, 1989, pp. 6–15.

[15] Bhattacharyya, A. K., "Generalised Transmission Line Model of Microstrip Patch Antennas and Some Applications," Ph.D. Thesis, Indian Institute of Technology, Kharagpur, India, 1985.

[16] Bhattacharyya, A. K., L. Shafai, and R. Garg, "Microstrip Antenna—A Generalised Transmission Line," *Progress in Electromagnetics Research*, Vol. 4, 1991, pp. 45–84.

[17] Bhattacharyya, A. K., and R. Garg, "A Microstrip Array of Concentric Annular Rings," *IEEE Trans. on Antennas and Propagation*, Vol. AP-33, 1985, pp. 655–659.

[18] Bhattacharyya, A. K., and L. Shafai, "Theoretical and Experimental Investigations of the Elliptical Annular Ring Antenna," *IEEE Trans. on Antennas and Propagation*, Vol. AP-36, 1988, pp. 1526–1530.

[19] Bhattacharyya, A. K., and L. Shafai, "A Wider Band Microstrip Antenna for Circular Polarization," *IEEE Trans. on Antennas and Propagation*, Vol. AP-36, 1988, pp. 157–163.

[20] Bhattacharyya, A. K., and R. Garg, "Self and Mutual Admittances Between Two Concentric, Coplanar, Circular Radiating Current Sources," *Proc. IEE*, Vol. 131, Pt. H, 1984, pp. 217–219.

[21] Bahl, I. J., and P. Bhartia, *Microstrip Antennas*, Artech House, Dedham, MA, 1980.

[22] Daniel, J. P., et al., "Research on Planar Antennas and Arrays: 'Structures Rayonnantes,' " *IEEE Antennas Propagation Magazine*, Vol. 35, Feb. 1993, pp. 14–38.

[23] Dubost, G., and A. Zerguerras, "Transmission-Line Model Analysis of Arbitrary Shape Symmetrical Patch Antenna Coupled With a Director," *Electron. Lett.*, Vol. 26, 1990, pp. 952–954.

[24] Dubost, G., et al., "Radiation of Arbitrary Shape Symmetrical Patch Antenna Coupled With a Director," *Electron. Lett.*, Vol. 26, 1990, pp. 1539–1540.

[25] Dubost, G., and A. Rabbaa, "Analysis of a Slot Microstrip Antenna," *IEEE Trans. on Antennas and Propagation*, Vol. AP-34, 1986, pp. 155–163.

[26] Dubost, G., *Flat Radiating Dipoles and Applications to Arrays*, John Wiley, New York, 1981.

[27] Schaubert, D. H., et al., "Effect of Microstrip Antenna Substrate Thickness and Permittivity: Comparison of Theories and Experiment," *IEEE Trans. on Antennas and Propagation*, Vol. AP-37, 1989, pp. 677–682.

[28] Lo, Y. T., et al., "Theory and Experiment on Microstrip Antennas," *IEEE Trans. on Antennas and Propagation*, Vol. AP-27, 1979, pp. 137–145.

[29] Richards, W. F., et al., "An Improved Theory for Microstrip Antennas and Applications," *IEEE Trans. on Antennas and Propagation*, Vol. AP-29, 1981, pp. 38–46.

[30] Lo, Y. T., and W. F. Richards, "Perturbation Approach to Design of Circularly Polarized Microstrip Antennas," *Electron. Lett.*, 1981, pp. 383–385.

[31] Carver, K. R., and J. W. Mink, "Microstrip Antenna Technology," *IEEE Trans. on Antennas and Propagation*, Vol. AP-29, 1981, pp. 2–24.

[32] Thouroude, D., et al., "CAD-Oriented Cavity Model for Rectangular Patches," *Electron. Lett., Vol. 26*, 1990, pp. 842–844.

[33] Richards, W. F., et al., "Theory and Applications for Microstrip Antennas," *Proc. Workshop Printed Circuit Antenna Tech.*, New Mexico State University, Las Cruces, NM, 1979, pp. 8/1–23.

[34] Long, S. A., et al., "Impedance of a Circular-Disc Printed-Circuit Antenna," *Electron. Lett.*, Vol. 14, 1978, pp. 684–686.

[35] Dahele, J. S., and K. F. Lee, "Effect of Substrate Thickness on the Performance of a Circular-Disc Microstrip Antenna," *IEEE Trans. on Antennas and Propagation*, Vol. AP-31, 1983, pp. 358–360.

[36] Lee, K. F., K. M. Luk, and J. S. Dahele, "Characteristics of the Equilateral Triangular Patch Antenna," *IEEE Trans. on Antennas and Propagation*, Vol. AP-36, 1988, pp. 1510–1818.

[37] Mink, J. W., "Circular Ring Microstrip Antenna Elements," *IEEE AP-S Int. Symp. Digest*, 1980, pp. 605–608.

[38] Lee, K. F., and J. S. Dahele, "Theory and Experiment on Annular-Ring Microstrip Antenna," *Ann. des Telecomm.*, Vol. 40, 1985, pp. 508–515.

[39] Richards, W. F., et al., "A Theoretical and Experimental Investigation of Annular Ring, Annular Sector and Circular Sector Microstrip Antennas," *IEEE Trans. on Antennas and Propagation*, Vol. AP-32, 1984, pp. 864–866.

[40] Lee, K. F., K. Y. Ho, and J. S. Dahele, "Circular-Disk Microstrip Antenna With an Air Gap," *IEEE Trans. on Antennas and Propagation*, Vol. AP-32, 1984, pp. 880–884.

[41] Dahele, J. S., K. F. Lee, and D. P. Wong, "Dual-Frequency Stacked Annular Ring Microstrip Antenna," *IEEE Trans. on Antennas and Propagation*, Vol. AP-35, 1987, pp. 1281–1285.

[42] Penard, E., and J. P. Daniel, "Mutual Coupling Between Microstrip Antennas," *Electron. Lett.*, Vol. 18, 1982, pp. 605–607.

[43] Himdi, M., et al., "Analysis of Aperture-Coupled Microstrip Antenna Using Cavity Method," *Electron. Lett.*, Vol. 25, 1989, 391–392.

[44] Ittipiboon, A., R. Oostlander, and Y. M. M. Antar, "Modal Expansion Method of Analysis for Slot-Coupled Microstrip Antenna," *Electron. Lett.*, Vol. 25, 1989, pp. 1338–1340.

[45] Palanisamy, V., "Generalized Cavity Model of Microstrip Patch Antennas and Some Applications," Ph.D. Thesis, Indian Institute of Technology, Kharagpur, India, 1985.

[46] Palanisamy, V., and R. Garg, "Analysis of Arbitrary Shaped Microstrip Patch Antennas Using Segmentation Technique and Cavity Model," *IEEE Trans. on Antennas and Propagation*, Vol. AP-34, 1986, pp. 1208–1213.

[47] Okoshi, T., *Planar Circuits for Microwaves and Lightwaves*, Springer Verlag, New York, 1985, Chap. 5.

[48] Palanisamy, V., and R. Garg, "Rectangular Ring and H-Shaped Microstrip Antennas—Alternatives to Rectangular Patch Antenna," *Electron. Lett.*, Vol. 21, 1985, pp. 874–876.

[49] Palanisamy, V., and R. Garg, "Analysis of Circularly Polarized Square Ring and Crossed-Strip Microstrip Antennas," *IEEE Trans. on Antennas and Propagation*, Vol. AP-34, 1986, pp. 1340–1346.

[50] Gupta, K. C., and A. Benalla, "Two-Port Transmission Characteristics of Circular Microstrip Patch Antennas," *IEEE AP-S Int. Symp. Digest*, 1986, pp. 821–824.

[51] Gupta, K. C., R. Garg, and R. Chadha, *Computer-Aided Design of Microwave Circuits*, Artech House, Dedham, MA, 1981.

[52] Benalla, A., and K. C. Gupta, "Multiport Network Approach for Modeling Mutual Coupling Effects in Microstrip Patch Antennas and Arrays," *IEEE Trans. on Antennas and Propagation*, Vol. AP-37, 1989, pp. 148–152.

[53] Gupta, K. C., "Two-Dimensional Analysis of Microstrip Circuits and Antennas," *J. Inst. Electron. Telecommun. Engrs. (India),* Vol. 28, 1982, pp. 346–364.

[54] Gupta, K. C., and P. C. Sharma, "Segmentation and Desegmentation Techniques for the Analysis of Two-Dimensional Microstrip Antennas," *IEEE AP-S Int. Symp. Digest*, 1981, pp. 19–22.

[55] Sharma, P. C., and K. C. Gupta, "Analysis and Optimized Design of Single Feed Circularly Polarized Microstrip Antennas," *IEEE Trans. on Antennas and Propagation*, Vol. AP-31, 1983, pp. 949–955.

[56] Kumar, G., and K. C. Gupta, "Broadband Microstrip Antennas Using Additional Resonators Gap-Coupled to Radiating Edges," *IEEE Trans. on Antennas and Propagation*, Vol. AP-32, 1984, pp. 1375–1379.

[57] Kumar, G., and K. C. Gupta, "Nonradiating Edges and Four-Edges Gap-Coupled Multiple Resonator, Broadband Microstrip Antennas," *IEEE Trans. on Antennas and Propagation*, Vol. AP-33, 1985, pp. 1375–1379.

[58] Kumar, G., and K. C. Gupta, "Directly Coupled Multiple Resonator Wideband Microstrip Antennas," *IEEE Trans. on Antennas and Propagation*, Vol. AP-33, 1985, pp. 588–593.

[59] Benalla, A., and K. C. Gupta, "Multiport Network Model and Transmission Characteristics of Two-Port Rectangular Microstrip Antennas," *IEEE Trans. on Antennas and Propagation*, Vol. AP-36, 1988, pp. 1337–1342.

[60] Parrikar, R. P., and K. C. Gupta, "Multiport Network Model for CAD of Electromagnetically Coupled Patch Antennas," *IEEE Trans. on Microwave Theory and Techniques*, Vol. MTT-46, 1998, pp. 475–483.

[61] Harrington, R. F., *Time-Harmonic Electromagnetic Fields*, McGraw-Hill, New York, 1961.

[62] Jackson, D. R., and N. G. Alexopoulos, "Simple Approximate Formulas for Input Resistance, Bandwidth, and Efficiency of a Resonant Rectangular Patch," *IEEE Trans. on Antennas and Propagation*, Vol. AP-39, 1991, pp. 407–410.

[63] James, J. R., P. S. Hall, and C. Wood, *Microstrip Antenna: Theory and Design*, Peter Peregrinus, London, UK, 1981.

[64] Sobol, H., "Radiation Conductance of Open-Circuit Microstrip," *IEEE Trans. on Microwave Theory and Techniques*, Vol. MTT-19, 1971, pp. 885–887.

[65] Van der Pauw, L. J., "The Radiation of Electromagnetic Power by Microstrip Configurations," *IEEE Trans. on Microwave Theory and Techniques*, Vol. MTT-25, 1977, pp. 719–725.

[66] Lewin, L., "Spurious Radiation From Microstrip," *Proc. IEE*, Vol. 125, 1978, pp. 633–642.

[67] James, J. R., and A. Henderson, "High Frequency Behaviour of Microstrip Open-Circuit Terminations," *IEE J. Microwave Optics & Acoustics*, Vol. 3, 1979, pp. 205–218.

[68] Chuang, C. L., et al., "The Equivalence of the Electric and Magnetic Surface Current Approaches in Microstrip Antenna Studies," *IEEE Trans. on Antennas and Propagation*, Vol. AP-28, 1980, pp. 569–571.

[69] Gogoi, A., and K. C. Gupta, "Wiener-Hopf Computation of Edge-Admittances for Microstrip Patch Radiators," *Arch. Elek. Ubertragung.*, Vol. 36, 1982, pp. 247–251.

[70] Kuester, E. F., et al., "The Thin-Substrate Approximation for Reflection From the End of a Slab-Loaded Parallel Plate Waveguide With Application to Microstrip Patch Antennas," *IEEE Trans. on Antennas and Propagation*, Vol. AP-30, 1982, pp. 910–917.

[71] Bhattacharyya, A. K., and R. Garg, "Effect of Substrate on the Efficiency of an Arbitrarily Shaped Microstrip Patch Antenna," *IEEE Trans. on Antennas and Propagation*, Vol. AP-34, 1986, pp. 1181–1188.

[72] Wolff, I., and N. Knoppik, "Rectangular and Circular Microstrip Disc Capacitors and Resonators," *IEEE Trans. on Microwave Theory and Techniques*, Vol. MTT-22, 1974, pp. 857–864.

[73] Katehi, P. B., and N. G. Alexopoulos, "Frequency-Dependent Characteristics of Microstrip Discontinuities in Millimeter-Wave Integrated Circuits," *IEEE Trans. on Microwave Theory and Techniques*, Vol. MTT-33, 1985, pp. 1029–1035.

[74] Jackson, R. W., and D. M. Pozar, "Full-Wave Analysis of Microstrip Open-End and Gap Discontinuities," *IEEE Trans. on Microwave Theory and Techniques*, Vol. MTT-33, 1985, pp. 1036–1042.

[75] Jansen, R. H., and N. H. L. Koster, "Accurate Results on the End Effect of Single and Coupled Microstrip Lines for Use in Microwave Circuits Design," *AEU*, Vol. 34, 1980, pp. 453–459.

[76] Kirschning, M., et al., "Accurate Model for Open-End Effect of Microstrip Lines," *Electron. Lett.*, Vol. 17, 1981, pp. 123–125.

[77] Lewin, L., "Radiation From Discontinuities in Stripline," *Proc. IEE,* Vol. 107C, 1960, pp. 163–170.

[78] Richards, W. F., et al., "Experimental and Theoretical Investigation of the Inductance Associated With a Microstrip Antenna Feed," *Electromagnetics*, Vol. 3, 1983, pp. 327–346.

[79] Damiano, J. P., and A. Papiernik, "Survey of Analytical and Numerical Models for Probe-Fed Microstrip Antennas," *IEE Proc. Microwaves, Antennas Propagation*, Vol. 141, 1994, pp. 15–22.

[80] Zheng, J. X., and D. C. Chang, "End-Correction Network of a Coaxial Probe for Microstrip Patch Antennas," *IEEE Trans. on Antennas and Propagation*, Vol. AP-39, 1991, pp. 115–118.

[81] Tulintseff, A. N., S. M. Al, and J. A. Kong, "Input Impedance of a Probe-Fed Stacked Circular Microstrip Antenna," *IEEE Trans. on Antennas and Propagation*, Vol. AP-39, 1991, pp. 381–390.

[82] Lewin, L., "A Contribution to the Theory of Cylindrical Antennas—Radiation Between Parallel Plates," *IRE Trans.*, Vol. AP-7, 1959, pp. 162–168.

[83] Fong, K. S., H. F. Pues, and M. J. Withers, "Wideband Multilayer Coaxial-Fed Microstrip Antenna Element," *Electron. Lett.*, Vol. 21, 1985, pp. 497–499.

[84] Dearnley, R. W., and A. R. F. Barel, "A Comparison of Models to Determine the Resonant Frequencies of a Rectangular Microstrip Antenna," *IEEE Trans. on Antennas and Propagation*, Vol. AP-37, 1989, pp. 114–118.

[85] Kumprasert, N., and W. Kiranon, "Simple and Accurate Formula for the Resonant Frequency of the Circular Microstrip Disk Antenna," *IEEE Trans. on Antennas and Propagation*, Vol. AP-43, 1995, pp. 1331–1333.

[86] Kumprasert, N., and W. Kiranon, "Simple and Accurate Formula for the Resonant Frequency of the Equilateral Triangular Microstrip Patch Antenna," *IEEE Trans. on Antennas and Propagation*, Vol. AP-42, 1994, pp. 1178–1179.

[87] Damiano, J.-P., J.-M. Ribero, and R. Staraj, "Original Simple and Accurate Model for Elliptical Microstrip Antennas," *Electron. Lett.*, Vol. 31, 1995, pp. 1023–1024.

[88] Rengarajan, S. R., "Resonance Frequency of Elliptical Microstrip Antennas," *Electron. Lett.*, Vol. 29, 1993, pp. 1066–1067.

[89] Singh, R., A. De, and R. S. Yadav, "Comments on an Improved Formula for the Resonant Frequency of the Triangular Microstrip Antenna," *IEEE Trans. on Antennas and Propagation*, Vol. AP-39, 1991, pp. 1443–1444.

[90] Chew, W. C., and J. A. Kong, "Effects of Fringing Fields on the Capacitance of Circular Microstrip Ring Antenna," *IEEE Trans. on Microwave Theory and Techniques*, Vol. MTT-28, 1980, pp. 98–104.

[91] Suzuki, Y., and T. Chiba, "Computer Analysis Method for Arbitrary Shaped Microstrip Antenna With Multi-Terminals," *IEEE Trans. on Antennas and Propagation*, Vol. AP-32, 1984, pp. 585–590.

[92] Mythili, P., and A. Das, "Simple Approach to Determine Resonant Frequencies of Microstrip Antennas," *IEE Proc. Microwaves, Antennas Propagation*, Vol. 145, 1998, pp. 159–162.